

**SECOND HARMONIC RAYLEIGH WAVE DETECTION USING A
HETERODYNE LASER INTERFEROMETER**

A Thesis
Presented to
The Academic Faculty

by

Aulon Bajrami

In Partial Fulfillment
of the Requirements for the Degree
Master of Science in Engineering Science and Mechanics in the
School of Civil and Environmental Engineering

Georgia Institute of Technology
August 2016

Copyright ©2016 Aulon Bajrami

SECOND HARMONIC RAYLEIGH WAVE DETECTION USING A
HETERODYNE LASER INTERFEROMETER

Approved by:

Professor Laurence J. Jacobs, Advisor
School of Civil and Environmental Engineering
Georgia Institute of Technology

Dr. Jin-Yeon Kim
School of Civil and Environmental Engineering
Georgia Institute of Technology

Dr. Jianmin Qu
Department of Civil and Environmental
Engineering
Northwestern University

Date Approved: 20. May 2016

ACKNOWLEDGEMENTS

First of all, I would like to express my appreciation to my advisor Professor Laurence J. Jacobs for the support and motivation he provided to me throughout my graduate studies. In addition to making it possible for me to come to Atlanta, he was always willing to provide a helpful hand during my year at Georgia Tech. He is also the reason why I was able to participate and present my work at the Quantitative Nondestructive Evaluation Conference in Minneapolis, Minnesota.

I also would like to thank Dr. Jin-Yean Kim for the excellent practical and professional help he shared with me in the field of non-destructive evaluation. He made this work possible by supporting me throughout the entirety of my research. I also want to thank Dr. Douglas B Williams for his assistance in the field of Digital Signal Processing. Thanks goes to Dr. Jianmin Qu from Northwestern University for serving as a committee member and reviewing this thesis. I would like to express special thanks to Prof. Lothar Gaul Sibylle Langer and Christian Ehrlich from the University of Stuttgart for choosing me as a candidate for the ISAP Program, which is finally supported by the DAAD.

I want to thank my lab-mates Katie Scott, Alexander Lakocy, Gun Kim and Mehdi Rashidi for providing an engaging and supportive atmosphere in the lab. Special thanks goes to David Torello for the advice and help he gave me throughout this thesis. Additionally, I would also like to gratefully acknowledge Tobias Oberhardt for sharing joy and sorrow with me during our year in Atlanta. Special thanks goes to my friends in Germany for always helping me whenever possible.

Moreover I want to express my deepest gratitude to my family, especially my brother Ardi Bajrami. His support has been invaluable to my success.

TABLE OF CONTENTS

ACKNOWLEDGEMENTS	iii
LIST OF TABLES	vi
LIST OF FIGURES	vii
LIST OF SYMBOLS OR ABBREVIATIONS	xi
SUMMARY	xii
I INTRODUCTION	1
1.1 Motivation	1
1.2 Objectives	2
1.3 Structure of the thesis	2
II WAVE PROPAGATION IN SOLIDS	4
2.1 Equation of Motion	4
2.2 Wave Phenomena	7
2.2.1 Plane Waves in an Unbound Medium	7
2.2.2 Harmonic waves	8
2.2.3 Wave Reflection at a Stress Free Boundary	8
2.3 Rayleigh Surface Waves	10
2.3.1 Properties of Rayleigh Waves	10
2.3.2 Excitation of Rayleigh Waves	11
2.4 Nonlinear Wave Propagation	12
2.4.1 Nonlinearity Parameter β	13
III MODULATION	17
3.1 Amplitude Modulation	17
3.1.1 Modulation Index	18
3.1.2 Spectrum and Bandwidth	18
3.2 Angle Modulation	19
3.2.1 Spectrum of an Angle-Modulated Signal	21
3.2.2 Properties of Bessel function of the first kind	24
3.2.3 Bandwidth	26

IV EXPERIMENTAL SETUP FOR THE SECOND HARMONIC GENERATION METHOD	28
4.1 Specimen	28
4.2 Function Generator	29
4.3 High Power Gated Amplifier	29
4.4 Oscilloscope	29
4.5 Transducer	30
4.6 Wedge	30
4.7 Detection System	30
4.8 Experimental Procedure	31
V SIGNAL PROCESSING	35
5.1 Demodulation	35
5.2 Nonideal Interferometer	36
5.2.1 Quadrature demodulation	36
5.2.2 Zero-cross detection	38
VI DATA ACQUISITION AND EXPERIMENTAL RESULTS AND INTERPRETATION	40
6.1 Output Signal	40
6.2 Quadrature demodulation scheme	41
6.3 Zero-crossing detection demodulation scheme	42
6.4 Comparison of the Results	43
VII CONCLUSION AND POSSIBLE IMPROVEMENTS	48
REFERENCES	50

LIST OF TABLES

2.1	Relationships between the angles of incident and reflected waves	9
3.1	Bessel Functions of the first kind	23
4.1	Material properties of modified 9 % Cr steel	29

LIST OF FIGURES

2.1	Momentum balance	5
2.2	Reflection of P-wave and SV-wave	9
2.3	particle motion of a Rayleigh wave	11
2.4	Refraction at boundary between wedge and specimen	12
2.5	Wave propagation in linear and nonlinear materials	13
2.6	Partial Displacement	13
3.1	Amplitude modulated signal in the time domain	18
3.2	Frequency spectrum of the AM signal	19
3.3	Angle modulation	22
3.4	Spectrum of frequency modulated signal	24
3.5	Bessel functions	26
4.1	Experimental setup for the second harmonic generation method	28
4.2	Wedge geometry	30
4.3	Schematic of Laser Detection System	31
4.4	Fundamental amplitude over the propagation distance	32
4.5	Qualitative nonlinearity contribution with increasing propagation distance	32
4.6	Colormap plot for the alignment of the propagation distance	33
4.7	Piezoelectric transducer and wedge mounted on the sample	34
5.1	Raw signal	36
5.2	Schematics of the quadrature demodulation	38
5.3	Complex projection of the fundamental amplitude	39
5.4	Interpolation between two sample points	39
6.1	Spectrum of the raw signal	40
6.2	Phase error of the measured signal	41
6.3	Spectrum of a mixed signal	42
6.4	Results for a quadrature demodulated signal	45
6.5	Demodulated time-domain signal showing 30 cycles of a received Rayleigh surface wave along with an approximate Hann window	46
6.6	Demodulated frequency-domain signal of a received Rayleigh surface wave	46

6.7 Results for a zero-crossing demodulated signal	47
--	----

LIST OF SYMBOLS OR ABBREVIATIONS

Symbol	Description
f_i	body force
C_{ijkl}	fourth order elastic tensor
C_{ijklmn}, M_{ijklmn}	higher order elastic tensor
E	Young's modulus
\mathbf{E}, E_{ij}	Lagrangian strain tensor
F	force
n_k	unit normal vector
S	surface
t_i	traction on surface
u_i	displacement
$\mathbf{u}, \mathbf{u}^{(n)}$	displacement vector
u_i	displacement
\ddot{u}_i	acceleration
V	volume
δ_{ij}	Kronecker delta
ϵ_{ij}	strain tensor
λ, μ	Lamé constants
ν	Poisson's ratio
ρ	material mass density
σ	longitudinal stress
σ_{ij}	Cauchy stress tensor
φ	scalar potential
Ψ	vector potential
ω	circular frequency
$\mathbf{p}, \mathbf{p}^{(n)}$	propagation direction vector

Symbol	Description
$\mathbf{d}, \mathbf{d}^{(n)}$	unit vector in direction of motion
c, c_n	wave velocity
t	time
\mathbf{x}, x_i	Lagrangian coordinate
\mathbf{x}', x'_i	Eulerian coordinate
c_L, c_T, c_R	longitudinal, transverse, Rayleigh wave velocity
t	time
k, k_n	wavenumber
T	cycle duration
θ_i	incident, reflection, transmission angle
A_n	wave amplitude
θ_{critical}	critical angle for Rayleigh wave excitation
A, B	amplitudes
k_R	longitudinal Rayleigh wavenumber
q, k	arbitrary constants
Λ	wavelength
β	nonlinearity parameter
\mathbf{I}	identity matrix
F_{ij}	deformation gradient
W	energy per unit mass
P_{ij}	Piola-Kirchhoff stress tensor
δ_{ij}	Kronecker delta
x_c	carrier signal
$\omega_c, \omega_f, \omega_p$	angular velocity of the carrier, angle modulated and phase modulated signal
$x_a, x_{\text{angle}}, x_p, x_f$	amplitude, angle, phase and frequency modulated signal
x_m, x_c	message, carrier signal

Symbol	Description
m_a	amplitude modulation index
$\phi_{angle}, \phi_p, \phi_f$	angle, phase, frequency deviation
θ_i	instantaneous phase
ω_i	instantaneous frequency
k_f, k_p	frequency, phase deviation constant
δ	Dirac delta function
P_r	power ratio
ζ, ζ_p, ζ_f	phase, frequency modulation index
BW	Bandwidth
c_n	Fourier coefficient

SUMMARY

Nonlinear acoustic measurements, including the generation of higher harmonics caused by nonlinear material behavior, have proven to be a useful technique to detect changes in the microstructure of a material, and thus, nondestructively characterize material state.

Optical detection of second harmonic Rayleigh waves by means of a heterodyne laser interferometer has advantages over traditional detection techniques such as contact transducers. Laser detection is a non-contact point measurement, which provides absolute readings of the surface displacements and the particle velocity of the Rayleigh surface waves. Frequency or phase modulation of the laser is caused by the Doppler effect on the velocity and displacement amplitudes of a vibrating specimen. This modulation can be recovered with suitable demodulators. This research explores digital demodulation techniques and their effects on higher harmonic measurements. A 9 % Cr ferretic martensitic steel is used to demonstrate the accuracy of the non-contact laser measurement. The results show that the second harmonic increase is hidden in wideband noise for this measurement setup and both, quadrature demodulation and zero-cross detection provide similar results.

CHAPTER I

INTRODUCTION

1.1 Motivation

Nonlinear ultrasonics waves have shown to be a useful technique to investigate higher harmonics caused by micro-structural changes and nonlinear material behavior. Unlike conventional nondestructive evaluation techniques which investigate individual cracks or features using a scattered wavefield, nonlinear methods provide the potential to quantify distributed damage in a micro scale and to detect micro-structural changes prior failure. Furthermore, nonlinear ultrasonics contribute to a fundamental understanding of the influence of micro-structural changes to the growth of material damage. Thereby the synergy of a propagation sinusoidal ultrasonic wave and the micro-structural features of a material generate a second harmonic wave, which is quantified by the acoustic nonlinearity parameter, β .

Second harmonic generation methods were first reported Breazeale et al. [12] [13] and the work by Gedroitz and Krasilnikov [2]. Since then this method has gained a significant attention in the literature and research. A relationship between the pinning of dislocations and the generation of higher harmonic components, has been shown by Hikata et al. [3], which was extended by Cantrell et al. [5]. These researchers tried to show the linear dependence of the generated second harmonic wave over the squared amplitude of the fundamental wave. In this research Rayleigh surface waves are used. Compared to bulk and shear waves, the diffraction and attenuation effect of Rayleigh waves is smaller and therefore they travel longer without a significant energy loss. They also do not require access of both sides of a specimen. So far, most of the research in the area of nonlinear ultrasonics has been concerned with a contact-wedge receiving setup. However, it has been shown that a contact wedge transducer setup tends to be inefficient and time consuming. Due to the inconsistent contact conditions at the wedge specimen interface. These circumstances have lead to the usage of an optical detection system of acoustic second harmonics using interferometric

techniques. This alternative provides absolute readings of the displacement and velocity. Since it is a non-contact method, it provides quick measurements, and requires little sample preparation.

Hurley [10] used a Michelson interferometer detection setup to perform nonlinear Rayleigh wave measurements. A comprehensive study of a laser heterodyne interferometer detection setup for nonlinear Rayleigh wave measurements has been provided by Herrmann [9]. He emphasizing the necessity of high system linearity of the exciting system and the surface quality of the specimen. This research considers a modified 9% Cr steel and tracks the second harmonics of Rayleigh waves as a function of propagation distance. In particular, Rayleigh waves and their basic features make them an ideal candidate for the investigation of micro-scale distributed damage with an optical detection technique using a heterodyne interferometer. However, the main disadvantage of an optical detection method is a limited sensitivity.

1.2 Objectives

The objective of this research is to develop modified digital demodulation techniques for the nonlinear Rayleigh wave measurement with a heterodyne laser interferometer optical detection setup, which does not add spurious second harmonics. Quadrature demodulation and Zero-crossing detection are the digital demodulation methods which are being applied in this research.

1.3 Structure of the thesis

This thesis starts with a brief overview of the fundamentals of wave propagation in solids, followed by the explanation of the characteristics of Rayleigh waves. Moreover the derivation of the nonlinearity parameter β for longitudinal waves and Rayleigh waves. Chapter 3 is a brief introduction into the basics of amplitude and angle modulation. Chapter 4 gives an insight in the experimental setup. In addition, a discussion about the experimental procedure of the nonlinear Rayleigh wave measurements using a heterodyne laser interferometer is provided. Continuing in this vein, Chapter 5 shows the theoretical approach of the necessary assumptions to process the ultrasonic data. It also provides a brief explanation

the the two different demodulation techniques, Quadrature demodulation and Zero-cross detection. Chapter 6 evaluates the results and compares the two demodulation schemes. Finally, Chapter 7 draws a conclusion and gives an outlook for future work.

WAVE PROPAGATION IN SOLIDS

Ultrasonic testing in elastic solids is based on time varying deformations in materials and provides a useful tool in Nondestructive Evaluation (NDE). Before giving a discussion about the experimental method, an overview of the physics and mathematics of the fundamentals of wave propagation in solids will be given in this chapter, based on Achenbach [1]. After deriving the equations of motion, the concepts of linear wave propagation phenomena lead to the introduction of Rayleigh surface waves. On this basis, the nonlinear stress-strain relationship in an elastic homogeneous material will be introduced to derive nonlinearity parameter.

2.1 Equation of Motion

A good point to start with is Newton's first law

$$F_j = m\ddot{u}_i. \tag{1}$$

For a body with the surface S enclosing the volume V, the balance of their linear momentum can be given by

$$\int_S t_i dS + \int_V \rho f_i dV = \int_V \rho \ddot{u}_i dV, \tag{2}$$

where t_i represents the traction on the Surface S, f_i the body forces, ρ the density and \ddot{u}_i denotes the second derivative of the displacement u_i with respect to time, as depicted in Figure 2.1. By substituting the Cauchy's stress formula

$$t_i = \sigma_{ij}n_k, \tag{3}$$

into σ_{ij} and making use of Gauss' theorem, we obtain a volume integral instead of a surface integral

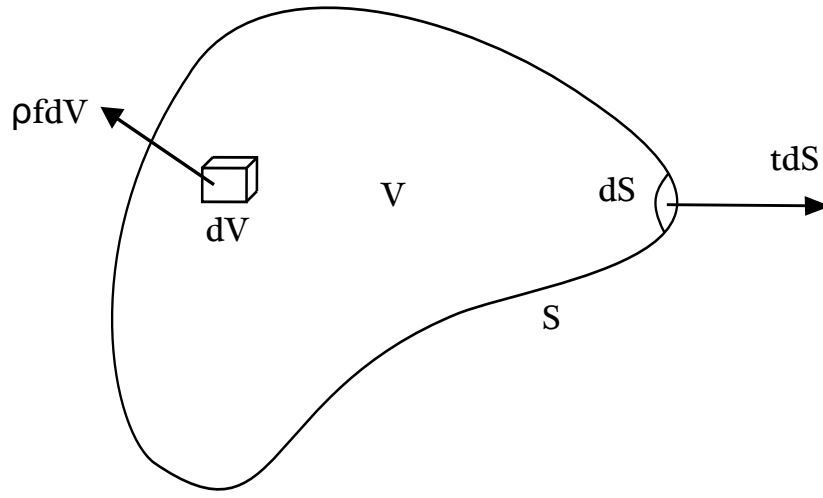


Figure 2.1: Momentum balance

$$\int_V (\sigma_{ij,j} + \rho f_i) dV = \int_V \rho \ddot{u}_i dV. \quad (4)$$

Since Equation 5, has to be valid for any arbitrary Volume, the localization argument should be used. This leads to Cauchy's first law of motion for a continuous integrand

$$\rho \ddot{u}_i = \sigma_{ij,i} + \rho f_i, \quad (5)$$

also known as linear momentum equation. The relationship between the strain ϵ_{ij} , and the displacement u_i , can be described by the compatibility equation

$$\epsilon_{ij} = \frac{1}{2}(u_{j,i} + u_{i,j}). \quad (6)$$

The general relationship between the stress and strain can be defined as

$$\sigma_{ij} = C_{ijkl} \epsilon_{ij}, \quad (7)$$

by using the fourth order stiffness tensor C_{ijkl} , which contains the mechanical properties of the material. However, sometimes it is desirable to define the equation of motion dependent of the material constants and displacement. Therefore, using Hooke's law simplifies the equation of motion into

$$\sigma_{ij} = \lambda \epsilon_{kk} \delta_{ij} + 2\mu \epsilon_{ij}, \quad (8)$$

defined by the Lamé constants

$$\lambda = \frac{E\nu}{(1+\nu)(1-2\nu)} \quad (9)$$

$$\mu = \frac{E}{2(1+\nu)}, \quad (10)$$

which can be obtained from the Poisson's ratio ν and the Young's modulus, E . Navier's equation of motion

$$(\lambda + \mu)u_{j,ji} + \mu u_{i,ji} = \rho \ddot{u}_i, \quad (11)$$

can be obtained by substituting Equation 6 and 7 into 5, which eliminates the stress and neglects the body forces. By using the identity

$$\nabla \nabla \cdot \mathbf{u} - \nabla \times \nabla \times \mathbf{u} = \nabla^2 \mathbf{u}, \quad (12)$$

we obtain the Navier's equation

$$\mu \nabla^2 \mathbf{u} + (\lambda + \mu) \nabla \nabla \cdot \mathbf{u} = \rho \ddot{\mathbf{u}}, \quad (13)$$

in a three-dimensional vector environment. Furthermore, it is possible to reduce Navier's equation into Helmholtz decomposition

$$\mathbf{u} = \nabla \varphi + \nabla \times \boldsymbol{\psi}, \quad (14)$$

where \mathbf{u} is represented by φ and $\boldsymbol{\psi}$. In order to guarantee a unique solution, the constraint

$$\nabla \cdot \boldsymbol{\psi} = 0, \quad (15)$$

has to be fulfilled. To derive the uncoupled equations in terms of φ and $\boldsymbol{\psi}$, we substitute Equation 14 and 15 into 13. This leads us to

$$(\lambda + 2\mu) \nabla^2 \varphi = \rho \ddot{\varphi} \quad (16)$$

and

$$\mu \nabla \psi = \rho \ddot{\psi}. \quad (17)$$

With the longitudinal wave speed

$$c_L = \sqrt{\frac{\lambda + 2\mu}{\rho}}, \quad (18)$$

and the transverse wave speed

$$c_T = \sqrt{\frac{\mu}{\rho}}, \quad (19)$$

we can derive the uncoupled wave equations

$$\nabla^2 \varphi = \frac{1}{c_L^2} \ddot{\varphi} \quad (20)$$

and

$$\nabla^2 \psi = \frac{1}{c_T^2} \ddot{\psi} \quad (21)$$

which represent longitudinal and shear waves, respectively.

2.2 Wave Phenomena

2.2.1 Plane Waves in an Unbound Medium

The general assumption of plane waves can be represented by

$$\mathbf{u} = f(\mathbf{x} \cdot \mathbf{p} - ct)\mathbf{d}, \quad (22)$$

where a wave with constant property values such as displacement \mathbf{u} , strain ϵ , and stress σ is propagating on a plane perpendicular to the propagation direction \mathbf{p} . The wave speed c , can hereby be defined as either the transverse wave speed c_T , or the longitudinal wave speed c_L . Furthermore, it is possible to obtain

$$(\mu - \rho c^2)\mathbf{d} + (\lambda + \mu)(\mathbf{p} \cdot \mathbf{d})\mathbf{p} = 0, \quad (23)$$

by substituting Equation 22 into 13, where \mathbf{p} and \mathbf{d} are defined as two unit vectors. Therefore, this equation is valid for following cases:

- The first case $\mathbf{d} = \pm\mathbf{p}$, implies that $\mathbf{p} \cdot \mathbf{d} = 1$. Thus, we can conclude that the waves and particles propagate in the same direction and the motion is therefore defined as a longitudinal P-wave. In this case, Equation 23 can be solved for the longitudinal wave speed $c = c_L = \sqrt{\frac{\lambda+2\mu}{\rho}}$.
- With the second case $\mathbf{p} \cdot \mathbf{d} = 0$, we assume a particle motion perpendicular to the propagation direction, which is known as a shear wave. For a shear wave, Equation (23) can be solved for the transverse wave speed $c = c_T = \sqrt{\frac{\mu}{\rho}}$.

2.2.2 Harmonic waves

It is useful to consider waves with a harmonic time behavior. Equation 22, can be also written as

$$\mathbf{u}^{(n)} = A_n \mathbf{d}^{(n)} e^{ik_n(\mathbf{x} \cdot \mathbf{p}^{(n)} - c_n t)}, \quad (24)$$

where the Amplitude A is neither depending on the position x nor the time t . Harmonic waves are plane waves with a phase velocity c and a given unit vector direction \mathbf{p} . $k_n = \frac{\omega}{c_n}$, is hereby defined as the wave number, where $\omega = \frac{2\pi}{T}$ denotes the circular frequency. The index n , is used to distinguish between a P- or SV-wave for the two dimensional case.

2.2.3 Wave Reflection at a Stress Free Boundary

The previous derived wave types are considered to propagate in an infinite medium. In reality, however, we encounter a finite medium where coupling and reflection will occur. In general, an incident P-wave will reflect into two reflected and two transmitted waves. In the case of a free boundary between a solid medium and vacuum, no transmission will occur and all the energy will be reflected inside the medium. Figure 2.2 shows the reflection created by an incident P- and SV-wave.

For a wave propagating in the x_1x_2 -plane, with a boundary orthogonal to the x_2 -axis, $\sigma_{22} = 0$ and $\sigma_{12} = 0$. One distinctive feature of the reflection is the effect of a single

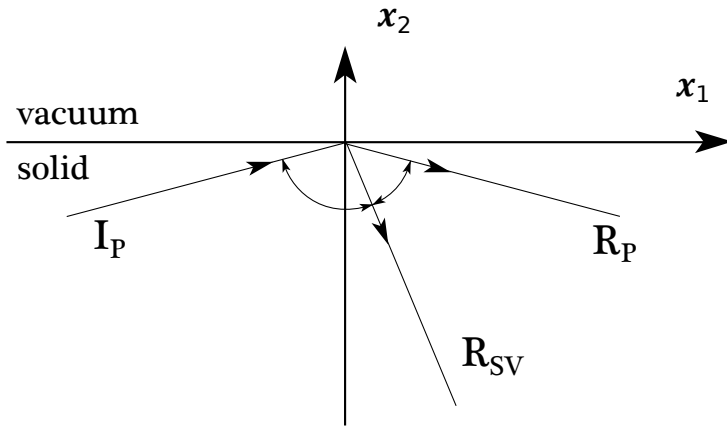


Figure 2.2: Reflection of P-wave and SV-wave

incident wave producing two different waves. Considering the fact that the frequency is constant for incident and reflected waves and taking advantage of the expression given in Equation 24, we obtain a correlation between the angles θ_0 , θ_1 and θ_2 , as shown in Table 2.1.

Table 2.1: Relationships between the angles of incident and reflected waves

Incident θ_0	Reflected P θ_1	Reflected SV θ_2
P	$\theta_1 = \theta_0$	$\sin \theta_2 = (c_T/c_L) \sin \theta_0$
SV	$\sin \theta_1 = (c_L/c_T) \sin \theta_0$	$\theta_2 = \theta_0$

The angles have to satisfy Snell's law

$$k_0 \sin \theta_0 = k_1 \sin \theta_1 = k_2 \sin \theta_2, \quad (25)$$

to obtain a non-trivial solution for the amplitudes A_n . For the special case of $\theta_0 = 0$ the wave will reflect itself since the incident wave is orthogonal to the boundary and no mode conversion will occur. No mode conversion occurs for the incident P-wave for the case of $\theta_0 > \theta_{critical}$. Thus, the reflected P-wave generates a wave which travels along the free surface and is generally known as a Rayleigh surface wave. Further properties for this specific harmonic wave can be found in Section 2.3.

2.3 Rayleigh Surface Waves

Rayleigh surface waves are described as a special type of acoustic surface waves that travel on solids. They are frequently used for the non-destructive evaluation of solid materials.

2.3.1 Properties of Rayleigh Waves

Rayleigh waves are surface waves and travel along a stress-free boundary. They include a phase shifted longitudinal and transversal motion which decays exponentially with depth, since it cancels out the stresses which they produce. The energy is therefore concentrated at the surface of an elastic solid material. The mathematical background and properties are provided in detail by Viktorov [18] and Achenbach [4]. By using the displacement potentials

$$\varphi = Ae^{-qx_3}e^{jk_R(x_1 - c_R t)} \quad (26)$$

and

$$\psi = Be^{-hx_3}e^{jk_R(x_1 - c_R t)}, \quad (27)$$

for a two-dimensional case we can describe the longitudinal and shear contributions of Rayleigh waves, where the variables A and B are defined as arbitrary constants and $q = \sqrt{1 - \left(\frac{c_R}{c_L}\right)^2}$, $h = \sqrt{1 - \left(\frac{c_R}{c_T}\right)^2}$. Furthermore, k_R is defined as the Rayleigh wavenumber with the relationship $k_R = \frac{\omega}{c_R}$, which provides the phase velocity of the Rayleigh wave. In order to obtain the characteristic equation

$$(h + k_R^2)^2 - 4hqk_R^2 = 0, \quad (28)$$

it is necessary to apply the stress-free boundary conditions into uncoupled wave equations, see Equation 20 and 21. Since the Rayleigh characteristic equation isn't dependent on the wavelength, we can conclude to a non-dispersive behavior according to Achenbach [4]. Furthermore, the Rayleigh wave speed can be obtained by using the approximation

$$c_R \approx \frac{0.862 + 1.14\nu}{1 + \nu}c_T, \quad (29)$$

where $\nu = 0.3$ is defined as the Poisson's ratio. Therefore we can conclude that the Rayleigh wave speed is in general slower than the phase velocity of shear and longitudinal waves, as described by Graff [7]. As it was mentioned, the particle motion of a propagation Rayleigh wave is a combination of longitudinal and shear displacement and shows an elliptical nature because the displacements along the vertical and horizontal axis are phase shifted by $\pi/2$, as depicted by Figure 2.3. Thereby, the ratio between the vertical and horizontal displacement is 3:2 and the particle motion of Rayleigh waves shows a retrospective behavior, i.e. the particles at the surface rotate counterclockwise, with respect to propagation direction. However, at a depth lower than approximately 0.192 times the wavelength Λ , the rotation direction changes into a clockwise rotation. As mentioned before, the energy of Rayleigh waves are concentrated near the free surface, which make them very sensitive to disturbances near the surface. Achenbach [4] also provided numerical solutions about the variations of the displacement with respect to depth. According to his results the amplitude of the displacement and the stresses are negligible at a depth lower than 1.5 times the wavelength. Therefore, the energy dissipation is much smaller compared to shear and longitudinal waves.

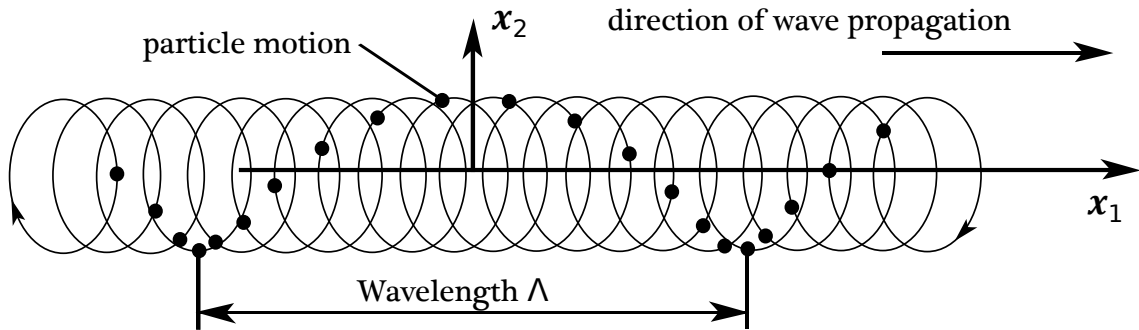


Figure 2.3: particle motion of a Rayleigh wave

2.3.2 Excitation of Rayleigh Waves

A normal ultrasonic transducer can generate either longitudinal or shear waves. One of the most common techniques to generate Rayleigh waves is to attach a longitudinal ultrasonic transducer on a wedge-shaped plastic body which is coupled to the surface of a solid or specimen. Thereby, the shape of the wedge and especially the angle θ_1 serves the role of

generating the Rayleigh waves due to the refraction between the wedge and the specimen. The required angle of the incident P-wave can be determined by using Snell's law

$$c_1 \sin \theta_2 = c_2 \sin \theta_1, \quad (30)$$

where c_1 and c_2 are defined as the incident and refraction wave velocities and θ_1 and θ_2 as their angles, see Figure 2.4.

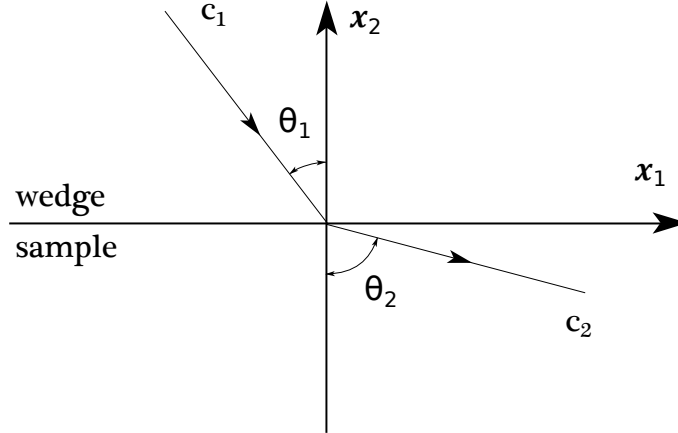


Figure 2.4: Refraction at boundary between wedge and specimen

Since Rayleigh waves travel along the surface, the angle of the refracted wave is given as $\theta_2 = \pi/2$ and the Rayleigh wave speed is $c_2 = c_R$. This leads to the critical angle

$$\theta_1 = \arcsin \left(\frac{c_L}{c_R} \right) \quad (31)$$

for a Rayleigh wave excitation with the longitudinal wave speed $c_1 = c_L$. This equation is only valid if c_L is smaller than c_R , which explains why the wave speed of the wedge material needs to be slower than the material of the specimen.

2.4 *Nonlinear Wave Propagation*

The wave propagation theory thus far, is based on an ideally linear stress-strain relationship. In reality, however, nonlinear distortion of the wave by the material leads to the generation of higher harmonic waves, as shown in Figure 2.5.

The amplitude of these higher harmonics, especially the second harmonic, can be used as an indicator for material damage, which makes this behavior useful for NDE. Thereby, the

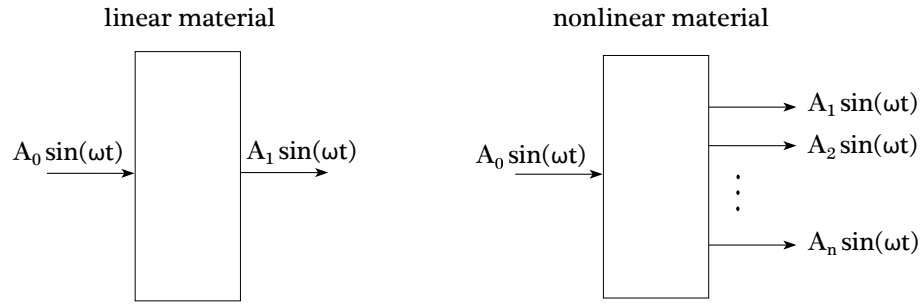


Figure 2.5: Wave propagation in linear and nonlinear materials

non-dimensional acoustic nonlinearity parameter β relates the amplitude of the first and second harmonic. Nonlinearity can be generated by means such as micro cracks, dislocations, vacancies, and precipitation. With increasing propagation distance the amplitude of higher harmonics increases. The following section provides an overview of nonlinear wave propagation in one-dimensional Rayleigh waves.

2.4.1 Nonlinearity Parameter β

As it was mentioned, the fundamental wave will distort as it propagates, higher harmonics will be generated and their nonlinearity is generally quantified by the nonlinearity parameter β , for which an expression is derived by Hamilton and Blackstock [8].

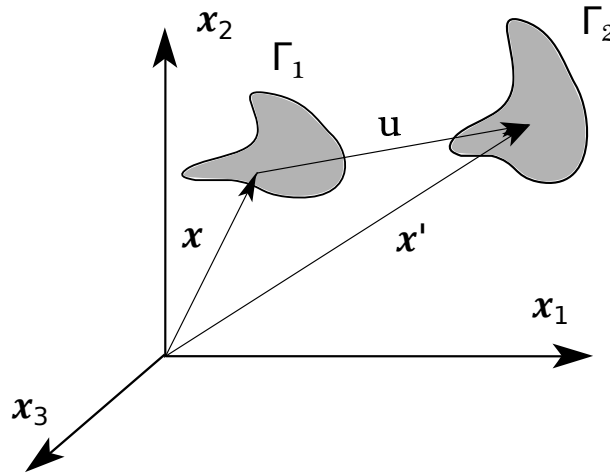


Figure 2.6: Partial Displacement

This section provides a summary of the main steps and an introduction to nonlinear wave propagation. By neglecting the body forces of the linear momentum in Equation 5, we can define the wave motion in an elastic solid as

$$\sigma_{ij,j} = \rho \frac{\partial^2 u_i}{\partial t^2}, \quad (32)$$

where the vector u_i denotes the particle displacement from the initial position to the displaced position and therefore $u_i = x'_i - x_i$. The transformation from the reference body Γ_1 , to the deformed body Γ_2 , can be mathematically described with the deformation gradient tensor

$$F_{ij} = \frac{\partial x'_i}{\partial x_j}, \quad (33)$$

see Figure 2.6. Furthermore, we can obtain the Lagrangian strain tensor

$$\mathbf{E} = \frac{1}{2} (\mathbf{F}^T \cdot \mathbf{F} - \mathbf{I}), \quad (34)$$

in vector notation and also in indicial notation

$$E_{ij} = \frac{1}{2} \left(\frac{\partial u_i}{\partial x_j} + \frac{\partial u_j}{\partial x_i} + \frac{\partial u_i}{\partial x_j} \frac{\partial u_j}{\partial x_i} \right). \quad (35)$$

The energy per unit mass W , depends only on volume change and local stretching and can be described as a function of the Lagrangian strain tensor

$$\rho_0 W = \frac{1}{2} C_{ijkl} E_{ij} E_{kl} + \frac{1}{6} C_{ijklmn} E_{ij} E_{kl} E_{mn} + \dots, \quad (36)$$

where C_{ijkl} and C_{ijklmn} are the second and third order order elastic constants. Now, the first Piola-Krichhoff stress tensor can be written as

$$P_{ij} = \rho_0 \frac{\partial W}{\partial F_{ij}}. \quad (37)$$

Substituting Equation 33 into 37, yields

$$P_{ij} = C_{ijkl} \frac{\partial u_k}{\partial x_l} + \frac{1}{2} M_{ijklmn} \frac{\partial u_k}{\partial x_l} \frac{\partial u_m}{\partial x_n} + \dots, \quad (38)$$

where $M_{ijklmn} = C_{ijklmn} + C_{ijln} \delta_{km} + C_{jnkl} \delta_{im} + C_{jlmn} \delta_{ik}$. With the relation between equation of motion for finite amplitude waves

$$P_{ij,j} = \rho_0 \frac{\partial^2 u_i}{\partial t^2}, \quad (39)$$

and Equation 37, we obtain

$$\rho_0 \frac{\partial^2 u_i}{\partial t^2} = \frac{\partial^2 u_k}{\partial x_j \partial x_l} \left(C_{ijkl} + M_{ijklmn} \frac{\partial u_m}{\partial x_n} + \dots \right), \quad (40)$$

which can be reduced to

$$\frac{\partial^2 u}{\partial t^2} = c_L^2 \frac{\partial^2 u}{\partial x^2} \left(1 - \beta \frac{\partial u}{\partial x} \right), \quad (41)$$

for the case of one-dimensional longitudinal waves with the nonlinearity parameter

$$\beta = - \left(\frac{3}{2} + \frac{C_{111}}{2\rho_0 c_L^2} \right). \quad (42)$$

The measurement method presented in the following chapters are amplitude based due to dislocation substructures. Therefore, it is useful to express the nonlinearity parameter β in terms of the harmonic displacement amplitudes, A_1 and A_2 . For a harmonic excitation of the form

$$u_0 \sin(\omega t - kx), \quad (43)$$

where $k = \frac{\omega}{c_L}$. Therefore, the nonlinear wave equation can be solves as

$$u = A_1 \sin(\omega t - kx) + A_2 \sin(2\omega t - 2kx), \quad (44)$$

which yields to

$$u = u_0 \sin(\omega t - kx) + \frac{\beta}{8} \left(\frac{\omega u_0}{c_L} \right)^2 x \sin(2\omega t - 2kx)u, \quad (45)$$

with the nonlinearity parameter

$$\beta = \frac{8c_L^2 A_2}{\omega^2 x A_1^2}. \quad (46)$$

The value of β , depends on the longitudinal wave speed c_L , the propagation distance x and the amplitude of the fundamental A_1 and second harmonic wave A_2 , which can be easily measured. This expression is only valid for one-dimensional longitudinal waves. However,

the the nonlinear parameter for Rayleigh waves differs only by a constant factor C , and therefore

$$\beta = \frac{A_2}{\omega^2 x A_1^2} C, \quad (47)$$

as shown by Herrmann et al [9]. The constant C is the value for a given material and it depends on the wave speeds, c_L and c_R .

CHAPTER III

MODULATION

The process of adding information signals to a high-frequency electronic or optical carrier signal is called modulation. Thereby, the carrier is defined as a signal with a steady waveform, constant amplitude and frequency. The information can be added by varying the amplitude, frequency or phase of the carrier, which are defined as amplitude, frequency and phase modulation, respectively. Modulation allows us to send a signal on higher frequency range and it is usually applied to electromagnetic signals, radio, optical lasers and computer networks. In this chapter an introductory overview of the mathematics of amplitude and angle modulation will be given, based on Young [19] and Ziemer [20].

3.1 Amplitude Modulation

The carrier signal

$$x_c(t) = A_c \cos \omega_c t, \quad (48)$$

can be defined as a sinusoidal continuous wave, where A_c is the amplitude and $\omega_c = 2\pi f_c$ is angular velocity of the carrier with the carrier frequency f_c . Hence, the mathematical representation of an amplitude modulated function can be written as

$$x_a(t) = (A_c + x_m(t)) \cos \omega_c t. \quad (49)$$

The sinusoidal message signal can be described by

$$x_m(t) = A_m \cos \omega_m t, \quad (50)$$

where A_m is the largest amplitude of the modulating signal and $\omega_m = 2\pi f_m$. Furthermore, the information of the message signal is in the envelope of the amplitude modulated function.

3.1.1 Modulation Index

Equation 49, defines A_c as a constant amplitude of the carrying signal. By increasing A_m , the amount of power in the message signal is being increased relative to the carrier signal. This ratio leads us to the mathematical definition of the modulation index

$$m_a = \frac{A_m}{A_c}, \quad (51)$$

for a amplitude modulated signal. Thus, we can express the modulated function as

$$x_a(t) = A_c (1 + m_a \cos \omega_m t) \cos \omega_c t. \quad (52)$$

Since $A_c \geq A_m$, the modulation index is limited between 0 and 1 and it can be defined as a percentage. Figure 3.1, shows an example of an amplitude modulated signal with the modulation index $m_a = 0.5$.

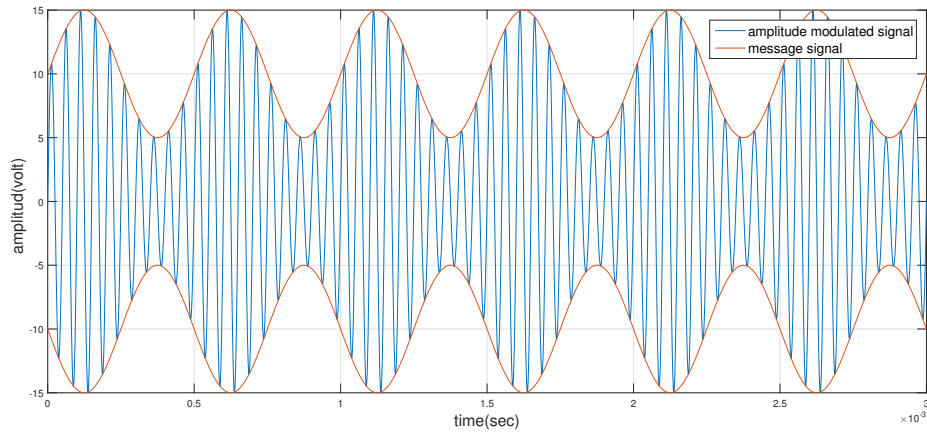


Figure 3.1: Amplitude modulated signal in the time domain

3.1.2 Spectrum and Bandwidth

The spectrum or also known as the frequency-domain, represents the relative energy components in dependency of the frequency. This enables us to see how the signal is varying in frequency domain, where the components are denoted as amplitudes in the frequency domain. By using the trigonometric identity $\cos x \cos y = \frac{1}{2} [\cos(x - y) + \cos(x + y)]$ and substituting it into

$$x_a(t) = A_c \cos \omega_c t + A_m \cos \omega_m t \cos \omega_c t, \quad (53)$$

the instantaneous amplitude of the signal can be represented by

$$x_a(t) = A_c \cos \omega_c t + \frac{1}{2} A_m \cos(\omega_c - \omega_m) t + \frac{1}{2} A_m \cos(\omega_c + \omega_m) t. \quad (54)$$

Therefore, the modulated signal has three components: the first term is the carrier, the second term containing the difference $\omega_c - \omega_m$ is the lower sideband and the third term containing the sum $\omega_c + \omega_m$ is the upper sideband.

$$x_a(f) = \frac{A_c}{2} (\delta(f - f_c) + \delta(f + f_c)) + \frac{A_m}{4} (\delta(f - (f_c - f_m)) + \delta(f + (f_c - f_m))) + \frac{A_m}{4} (\delta(f - (f_c + f_m)) + \delta(f + (f_c + f_m))) \quad (55)$$

Figure 3.2, shows the frequency spectrum of a amplitude modulated signal in terms of Dirac delta functions and so illustrates Equation 55.

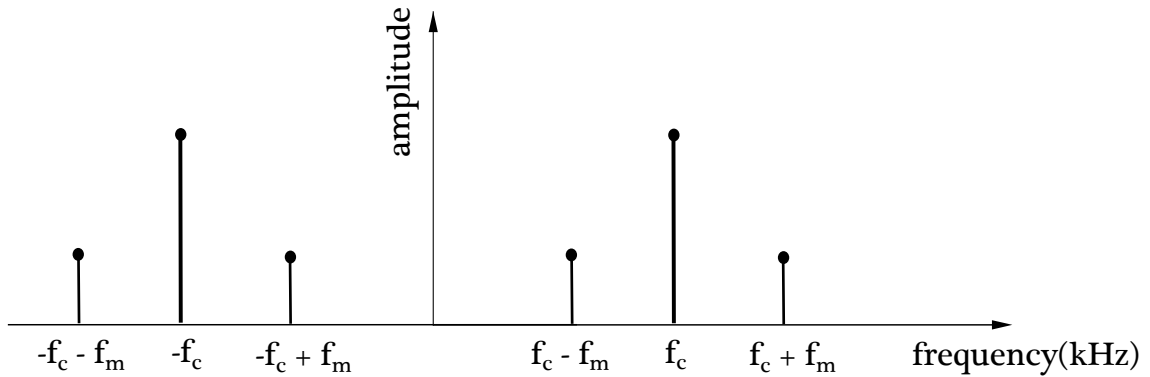


Figure 3.2: Frequency spectrum of the AM signal

3.2 Angle Modulation

In this type of modulation, the amplitude of the modulated signal remains constant which is considered to be the greatest advantage of angle modulation as reported by Kennedy et al. [11]. The angle varies proportionally to the amplitude of the message signal with respect to time. Thus, an angle modulated signal can generally be expressed by

$$x_{angle}(t) = A_{angle} \cos(\omega_c t + \phi_{angle}(t)), \quad (56)$$

where A_{angle} is defined as constant amplitude. The two different types of angle modulation, frequency modulation and phase modulation, can be distinguished by the type of deviation of the carrier proportional to the message signal. For the case of phase deviation

$$\phi_p(t) = k_p x_m(t), \quad (57)$$

we have a phase modulated signal, where the instantaneous phase of the modulated signal is defined as

$$\theta_i(t) = \omega_c t + \phi_p(t), \quad (58)$$

and k_p denotes the deviation constant. Similarly, frequency modulation can be identified by the frequency deviation

$$\frac{d\phi_f(t)}{dt} = k_f x_m(t), \quad (59)$$

with the instantaneous frequency

$$\omega_i(t) = \frac{d\theta_i}{dt} = \omega_c + \frac{d\phi_f(t)}{dt}. \quad (60)$$

In order to find the phase deviation of a frequency-modulated carrier, $\omega_i(t)$ must be integrated with respect to time. Thus

$$\phi_f(t) = k_f \int_{t_0}^t x_m(s) ds + \phi_0, \quad (61)$$

in which ϕ_0 is the phase deviation at $t = t_0$ and k_f is the the frequency deviation constant.

With these definitions we can express the output of a phase modulated signal

$$x_p(t) = A_p \cos(\omega_c t + k_p x_m(t)), \quad (62)$$

and the output of a frequency modulated signal

$$x_f(t) = A_f \cos \left(\omega_c t + k_f \int_{-\infty}^t x_m(s) ds \right). \quad (63)$$

3.2.1 Spectrum of an Angle-Modulated Signal

Since the two basic types of angle modulation are nonlinear, it is rather difficult to calculate the exact spectrum for general message signals. A possible study of the spectrum can be obtained by using a sinusoidal message signal $x_m(t) = A_m \cos w_m t$. Thus, we gain the phase deviation

$$\phi_p(t) = \zeta_p \cos w_m t, \quad (64)$$

for a phase modulated signal and also the frequency deviation

$$\phi_f(t) = \zeta_f \sin w_m t. \quad (65)$$

The parameter ζ denotes the modulation index for an angle modulated signal and stands for the maximum value of the phase deviation for both phase modulation $\zeta_p = k_p A_m$ and frequency modulation $\zeta_f = \frac{k_f A_m}{\omega_m}$. If we apply these conditions, the phase modulated signal is

$$x_p(t) = A_p \cos(\omega_c t + \zeta_p \cos w_m t), \quad (66)$$

and frequency modulated signal is

$$x_f(t) = A_f \cos(\omega_c t + \zeta_f \sin w_m t). \quad (67)$$

Comparing Equation 66 and 67 shows, that both equations are almost identical, the only difference is the modulation pattern. For the case of a sinusoidal message signal it causes a $\pi/2$ phase shift due to the differential of the message signal $x_m(t)$. Thus, there is no essential difference between the phase and frequency modulation. This comparison is illustrated in Figure 3.3, with the same carrier frequency f_c and the same value of the modulation index ζ for a phase and frequency modulated signal. For the sake of convenience, we

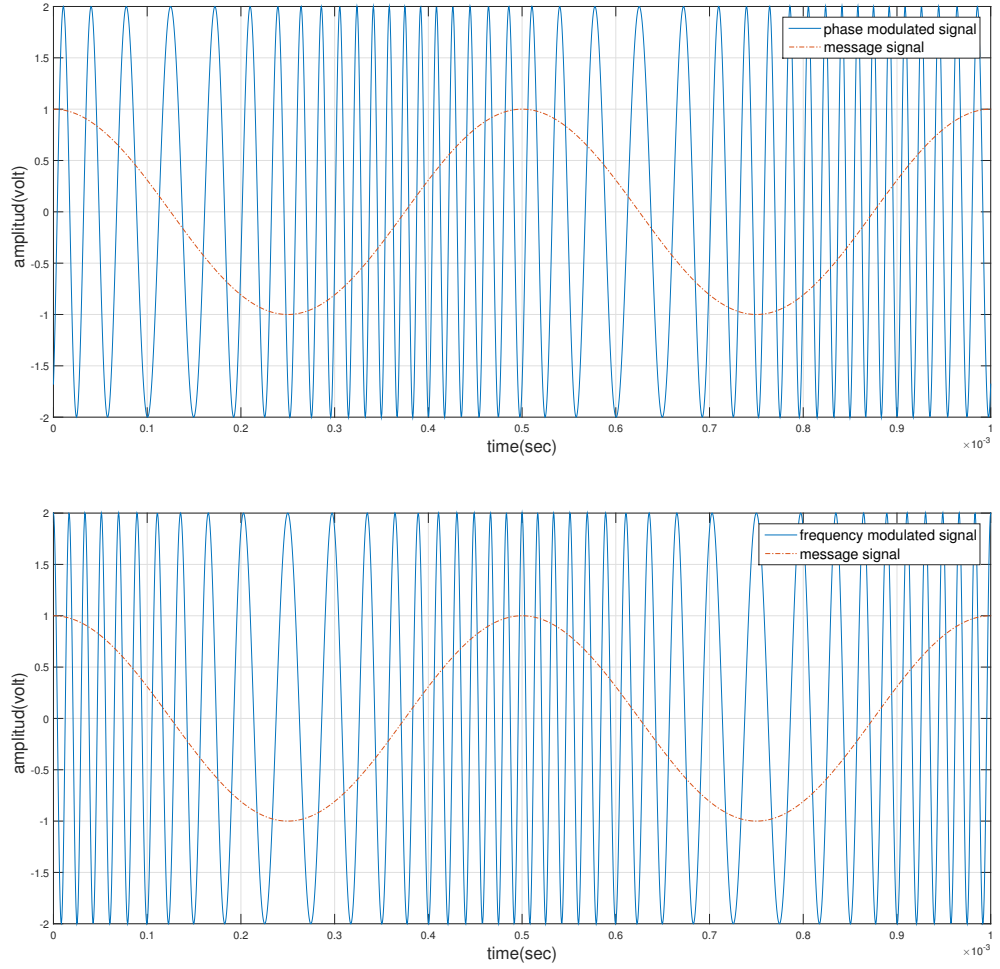


Figure 3.3: Angle modulation

will devote considerable attention to the term frequency modulation, which will include both modulation types in the analysis of the spectrum of angle modulation. By using an exponential representation of Equation 67

$$x(t) = A \operatorname{Re} \left\{ e^{j\omega_c t} e^{j\zeta \sin \omega_m t} \right\}, \quad (68)$$

it is possible represent the the complex periodic component as a Fourier series

$$e^{j\zeta \sin \omega_B t} = \sum_{n=-\infty}^{\infty} c_n e^{-jn\omega_n t}, \quad (69)$$

where we gain the Fourier coefficient [16]

$$c_n = \frac{1}{2\pi} \int_{-\pi}^{\pi} e^{j(\zeta \sin(x) - nx)} dx, \quad (70)$$

periodic in n with $w_m t = x$. This integral is also known as the Bessel function of the first kind, denoted as $J_n(\zeta)$ and a solution of the differential equation

$$\zeta^2 \frac{d^2 y}{d\zeta^2} + \zeta \frac{dy}{d\zeta} + (\zeta^2 - n^2) y(\zeta) = 0. \quad (71)$$

Table 3.1 shows several results of $J_n(\zeta)$ for different values of ζ and the natural number n .

Table 3.1: Bessel Functions of the first kind

ζ	J_0	J_1	J_2	J_3	J_4	J_5	J_6
0	1.00	-	-	-	-	-	-
0.25	0.98	0.12	-	-	-	-	-
0.5	0.94	0.24	0.03	-	-	-	-
1.0	0.77	0.44	0.11	0.02	-	-	-
1.5	0.51	0.56	0.23	0.06	0.01	-	-
2.0	0.22	0.58	0.35	0.13	0.03	-	-
3.0	-0.26	0.34	0.49	0.31	0.13	0.04	0.01

A proper explanation of the significance and the properties of Bessel functions of the first kind will be given later. By substituting Equations 69 and 70 into 68, we obtain

$$x(t) = A \operatorname{Re} \left\{ \sum_{n=-\infty}^{\infty} J_n(\zeta) e^{j(\omega_c + n\omega_m)t} \right\}. \quad (72)$$

Taking the real part yields to

$$x(t) = A \sum_{n=-\infty}^{\infty} J_n(\zeta) \cos(\omega_c + n\omega_m)t. \quad (73)$$

With the aid of the Fourier transform, we therefore obtain the discrete frequency modulated output

$$x(f) = \frac{A}{2} \sum_{n=-\infty}^{\infty} J_n(\zeta) (\delta(f - f_c - nf_m) + \delta(f + f_c + nf_m)). \quad (74)$$

Thereby the magnitude coefficients are displayed by Dirac delta functions proportional to $J_n(\zeta)$. Equation 74, enables us to compute the spectrum of a frequency modulated signal,

see Figure 3.4. Unlike the case of amplitude modulation, frequency modulation has an infinite number of sidebands with the carrier component.

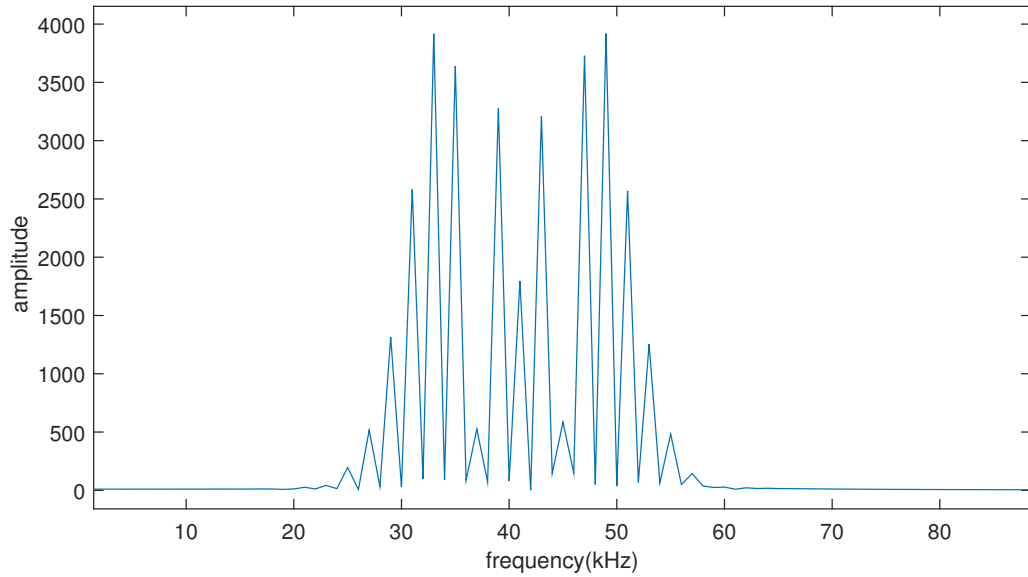


Figure 3.4: Spectrum of frequency modulated signal

3.2.2 Properties of Bessel function of the first kind

In order to evaluate the magnitude of the carrier and sidebands, it is necessary to determine the value of the corresponding Bessel function. This function cannot be expressed in closed form, see Equation 69. Various aspects of Bessel functions are very well studied in a large number of reference books and its values are documented in tables, similar to Table 3.1. However, there are some properties which need to be addressed due to their relevance to the spectrum of an angle modulated signal [11].

1. From the definition, it can be shown that sidebands are symmetrically distributed around the carrier frequency, which indicates a phase shift of π . Therefore it can be determined that

$$\begin{aligned}
 J_n(\zeta) &= (-1)^n J_{-n}(\zeta) \\
 &= \begin{cases} J_n(\zeta), & \text{for } n \text{ even} \\ -J_{-n}(\zeta), & \text{for } n \text{ odd} \end{cases} \quad (75)
 \end{aligned}$$

2. Due to the nature of Bessel functions it can be shown that for any value of ζ

$$\sum_{n=-\infty}^{\infty} J_n^2(\zeta) = 1. \quad (76)$$

3. For $\zeta \ll 1$, we can use the approximations $\cos \zeta = 1$ and $\sin \zeta \approx \zeta$. Under this condition $J_0(\zeta)$ and $J_1(\zeta)$ dominate the spectrum, i.e.

$$\begin{aligned} J_0(\zeta) &\approx 1 \\ J_1(\zeta) &\approx \frac{\zeta}{2} \\ J_n(\zeta) &\approx 0, \text{ for } n \geq 2 \end{aligned} \quad (77)$$

Therefore, the spectral components will be primarily the carrier frequency and the sidebands $J_1(\zeta)$ and $J_{-1}(\zeta)$. It is very similar to the spectrum of an amplitude modulated signal, with the exception of the phase reversal of the lower sideband component, as shown in Equation 75. This condition is also known as narrowband angle modulation.

4. For certain values of the modulation index $\zeta \approx 2.4$, $\zeta \approx 5.7$, $\zeta \approx 8.6$, for example. The carrier component disappears and all the energy is represented in the sidebands only. Whereas, for large values of ζ , energy is equally distributed in a large number of sidebands.

5. Directly from the definitions, we also get

$$\cos(\zeta \sin \theta) = J_0(\zeta) + 2 \sum_{n=1}^{\infty} J_{2n}(\zeta) \cos 2n\theta, \quad (78)$$

and

$$\sin(\zeta \sin \theta) = 2 \sum_{n=1}^{\infty} J_{2n-1}(\zeta) \sin((2n-1)\theta). \quad (79)$$

6. Lastly, a recursive relationship is satisfied by the Bessel functions

$$J_{n-1}(\zeta) + J_{n+1}(\zeta) = \frac{2n}{\zeta} J_n(\zeta), \quad (80)$$

with respect to each other. Thus, we can compute $J_{n+1}(\zeta)$ for a given value of ζ and the knowledge of $J_n(\zeta)$ and $J_{n-1}(\zeta)$.

Figure 3.5 illustrates the behavior of the Bessel functions, respectively most of the mentioned properties can be observed in this figure.

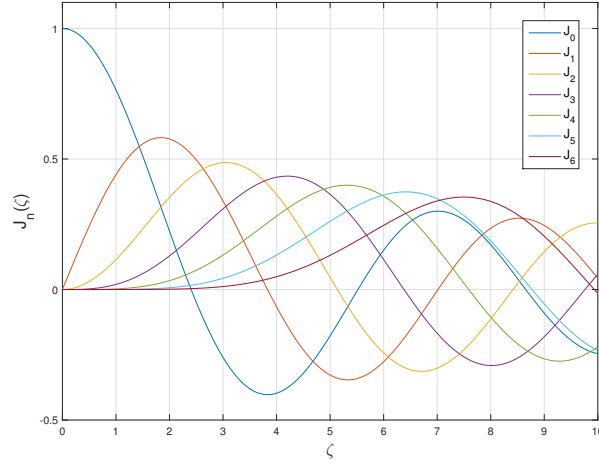


Figure 3.5: Bessel functions

3.2.3 Bandwidth

Based on Equation 74, the bandwidth of a frequency modulated signal is infinite. In practice however, the sideband amplitudes become negligibly small beyond a certain frequency offset from the carrier

$$\lim_{n \rightarrow \infty} J_n(\zeta) = 0. \quad (81)$$

Hence, for a particular application the bandwidth can be determined by considering sidebands which contain significant power. The relative amplitude and number of significant spectral components depend on ζ . As already mentioned, for a narrowband signal only $J_0(\zeta)$ and $J_1(\zeta)$ are significant. For $\zeta \gg 1$ however, the number of significant spectral components is large. Such a signal is known as wideband frequency modulation. The range of the bandwidth can be defined by using a power ratio P_r , i.e. the ratio of the power contained in the actual signal to the total power of the signal

$$P_r = \frac{\frac{1}{2}A^2 \sum_{n=-k}^k J_n^2(\zeta)}{\frac{1}{2}A^2 \sum_{n=-\infty}^{\infty} J_n^2(\zeta)}. \quad (82)$$

Alternatively it can be simplified into

$$P_r = J_0^2(\zeta) + 2 \sum_{n=1}^k J_n^2(\zeta), \quad (83)$$

by using the properties of the Bessel functions given in the previous chapter. For a given application, it is generally accepted to contain 98 % of its power. Therefore, we can approximate the bandwidth of a frequency modulated signal for the required value of k using a table of Bessel functions

$$\text{BW} = 2(\zeta + 1) f_m. \quad (84)$$

In the literature this expression is generally referred to as Carson's rule.

**EXPERIMENTAL SETUP FOR THE SECOND HARMONIC
GENERATION METHOD**

The following chapter will provide a basic overview of the experimental setup and equipment needed to generate and detect nonlinear Rayleigh surface waves. Furthermore, in this chapter a detailed model of the Laser Doppler Vibrometer (LDV), is introduced and the procedure for the second harmonic generation using Rayleigh surface waves, will be discussed in detail. Figure 4.1, illustrates the theoretical framework.

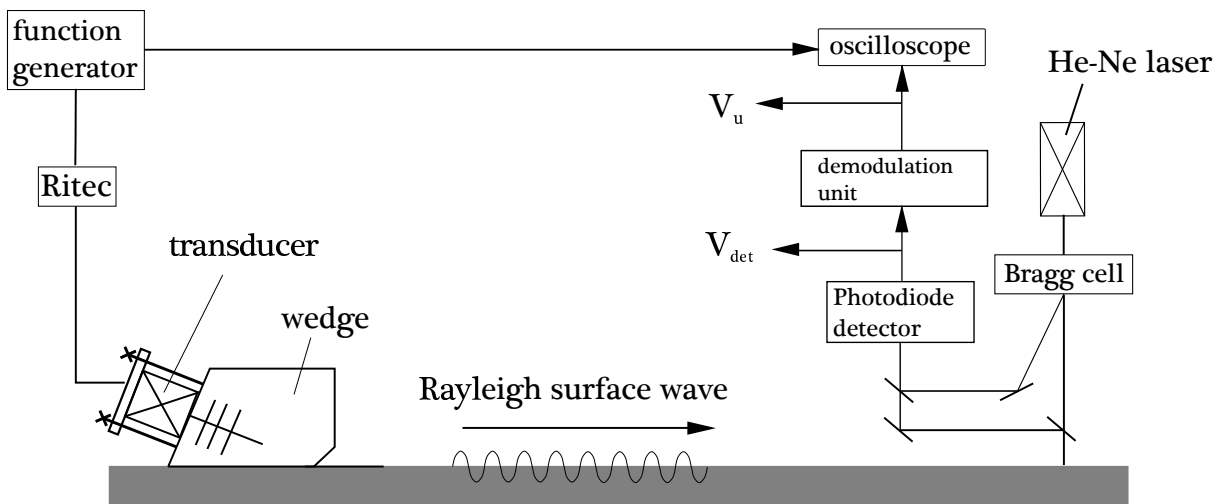


Figure 4.1: Experimental setup for the second harmonic generation method

4.1 Specimen

The material used in this research is 9 % Cr ferretic martensitic steel and it is used to demonstrate the accuracy of the non-contact laser measurement since there are results available for comparison provided by Marino at al. [14]. It has a length of 8 inches, width of 1.8 inches and a thickness of 0.5 inches. The specimen is hand polished after the grinding using a 2000 grade sandpaper to obtain reflective surface condition and remove all all visible texture effects, which leads to a better signal to noise ratio (SNR). The Material properties

of the modified 9% Cr steel are listed in Table 4.1 [6].

Table 4.1: Material properties of modified 9 % Cr steel

Yield strength	620MPa
Tensile strength R_m	755MPa
Elongation A_{50}	26%
Vickers hardness	235 HV10

4.2 *Function Generator*

The function generator is used to obtain a sinusoidal tone burst with a frequency of 2.1 MHz and a peak to peak voltage of 800 mV. An exciting signal containing 30 cycles ensures a sufficiently long steady state portion, which is necessary for the subsequent signal processing. The function generator has an internal trigger, which synchronizes the source with the amplifier and the oscilloscope.

4.3 *High Power Gated Amplifier*

By amplifying the output signal of the function generator with a high power amplifier (RITEC RAM-5000 Computer Controlled Ultrasonic System), we obtain the desired high-voltage excitation signal for the generating transducer. It is desirable, to introduce a high excitation signal to provide a good signal SNR for the second harmonic component at the receiver. The output level is set to 100% of the maximum capacity to provide for a sufficiently large amplitude. To ensure a stable output signal, the device remain tuned on for 30 minutes before continuing the measurement procedure. The amplifier itself introduces a certain inherent nonlinearity.

4.4 *Oscilloscope*

The signals are recorded with a Tektronix TDS 5034B digital oscilloscope at a sampling rate of 125 MS/s. The data was saved with a Labview script to import and post process the measured signals in Matlab.

4.5 *Transducer*

The experiments are conducted with an half-inch Panametrics V-type transducer with a nominal center frequency of 2.25 MHz, to generate longitudinal waves in an acrylic wedge. It has to be noted, that piezoelectric transducers induce a small amount of inherent non-linearity [9].

4.6 *Wedge*

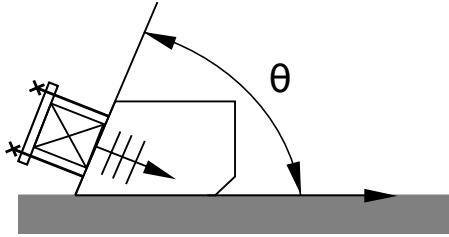


Figure 4.2: Wedge geometry

The wedge method is one of the most common methods to generate Rayleigh surface waves. The principle of this method is based upon introducing longitudinal waves into an acrylic wedge. In the contact area of the two bodies, the emitted waves from the transducer convert into Rayleigh waves. According to Achenbach [4], we obtain the phase velocity of a Rayleigh wave c_R by using the approximate solution, given in Equation 31. Thus, $c_R = 2964\text{m/s}$, for a Poisson's ratio of $\nu = 0.3$ and a transverse wave speed of 3200 m/s for steel. Furthermore, we gain the required wedge angle $\theta \approx 66.6$.

4.7 *Detection System*

The basic theoretical principles interferometers have been extensively studied and are described in the literature. A common type of optical interferometer is the Michelson interferometer. It is used as a non-contact vibration measurement of the surface and provides absolute values of the displacement, wide dynamic range and wide bandwidth. One of the most common types of the LDV is the heliumneon laser. Figure 4.3, illustrates the schematics of the Polytec OFV-534 Compact Sensor Head.

The present laser interferometer includes a laser unit and a sensor head. It works with a

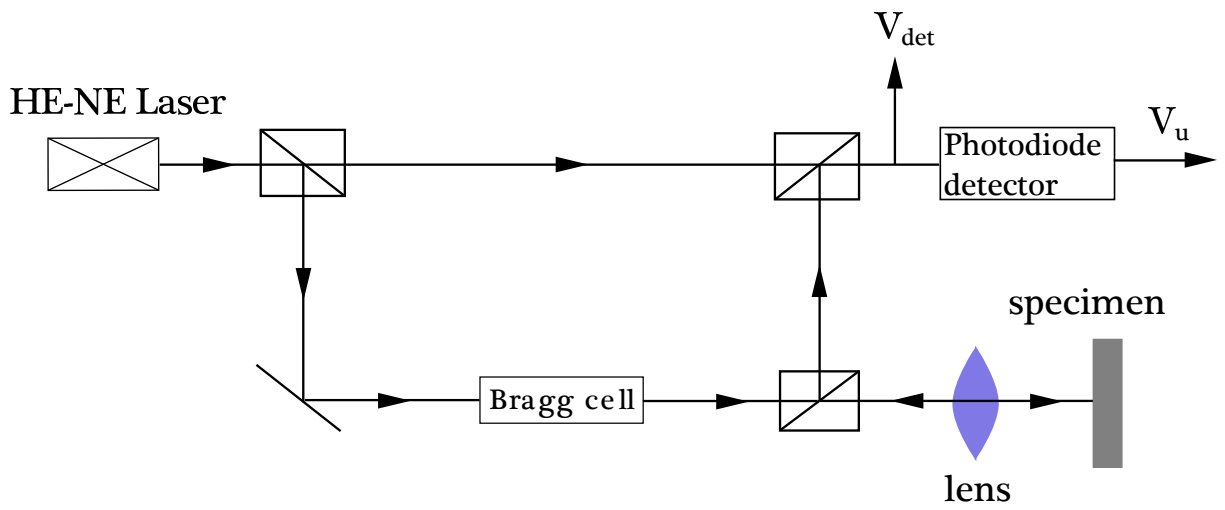


Figure 4.3: Schematic of Laser Detection System

Helium-Neon laser with a wavelength of 633 nm and delivers a vertically polarized light along an optical fiber to a high precision interferometer in the vibrometer head [1]. The Polytec LDV is designed for high optical sensitivity with a high resolution and broad bandwidth up to 24 MHz . A beam splitter, divides the laser light into a measurement beam and a reference beam, producing two beams with equal intensity. The measurement beam is directed at the surface of interest and contains the vibration amplitude and frequency of the specimen. The back scattered light is shifted slightly in frequency by the Doppler effect, which contains the absolute particle velocity and displacement on the surface of the specimen. The reference beam passes through the Bragg cell, which adds a frequency shift of 40 MHz . Due to interference between the measurement beam and the reference beam, a photo detector converts the optical signal into a standard frequency modulated signal.

Figure 4.4 shows the fundamental amplitude, conducted by using the experimental procedure, given in the following chapter. The data point along the propagation axis show for A_1 a decreasing trend, which can be explained by the attenuation and diffraction affect.

4.8 *Experimental Procedure*

As shown in Figure 4.7, a ultrasonic generation transducer combined with a wedge is positioned and fixed with a clamp on a specimen. To ensure an optimal transmission of the waves, light lubricant oil is used as an acoustic couplant between transducer-wedge and

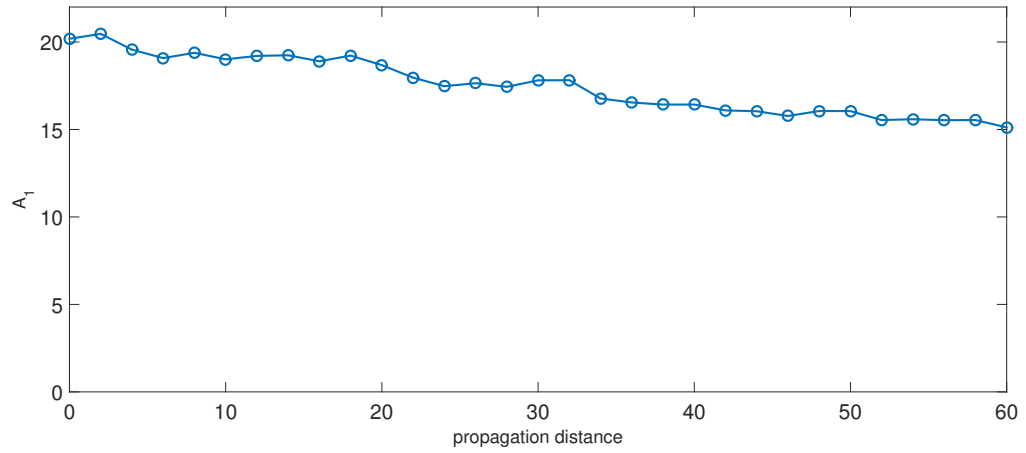


Figure 4.4: Fundamental amplitude over the propagation distance

wedge-specimen. Due to capillary action, the transmission characteristic changes over time. Therefore, it is necessary to give the couplant at least 30 minutes to settle in.

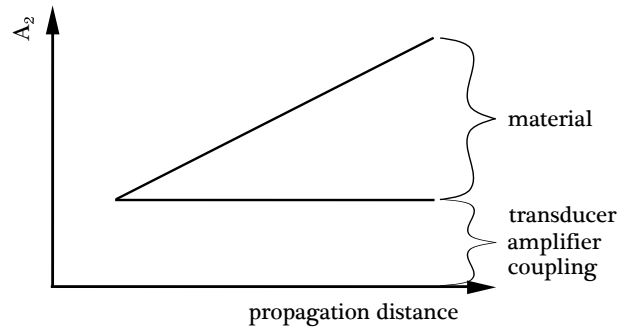


Figure 4.5: Qualitative nonlinearity contribution with increasing propagation distance

As it was mentioned, the electrical system used for the measurement procedure is a potential source of spurious higher harmonics. Likewise, the coupling condition is contributing to an increase of the nonlinearity. Furthermore, the amount of the second harmonic component introduced by the system nonlinearity increases with respect to the input voltage [17], which is the reason why a change in propagation distance is useful to measure the material nonlinearity. As depicted in Figure 4.5, the second harmonic generation due to electrical devices, has a constant influence on the measured material nonlinearity.

By scanning the surface of the specimen with laser vibrometer, starting from the wedge closest to the contact point between the wedge and the surface in propagation direction. Observation reveals that the Rayleigh wave beam does not come directly out of the middle

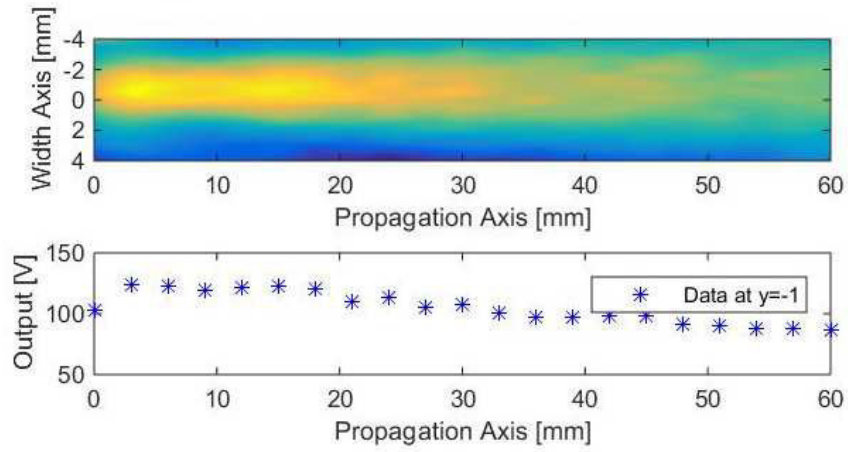


Figure 4.6: Colormap plot for the alignment of the propagation distance

of the exciting wedge. In order to determine the acoustic path, a calibration procedure has to be conducted. The effect of misalignment can be seen in Figure 4.6, which shows particle displacement of the surface. Thereby, we can observe an offset and an angle difference between the expected and the actual propagation axis. This calls for localization of the maximum amplitude at the beginning and the end of the propagation distance, achieved by scanning these positions parallel to the transducer plane. They were chosen between $x_{min} = 0mm$ and $x_{max} = 60mm$. For the calibration, the internal demodulation scheme of the OFV-551 fiber optic sensor head was used, as it provides accurate results for the fundamental frequency components. Higher harmonic Rayleigh wave measurements however, require that suitable digital demodulation techniques need to be applied. Measurements are taken along the actual propagation axis, in increments of 2 mm by moving the heterodyne laser interferometer and observing the raw modulated signal. It is not possible to average the observed signal with the Oscilloscope since it eliminates the carrier. Furthermore, we need to take several snapshots for every increment along the propagation axis to apply an averaging tool in the post processing section. Further application will be discussed in the following chapter.

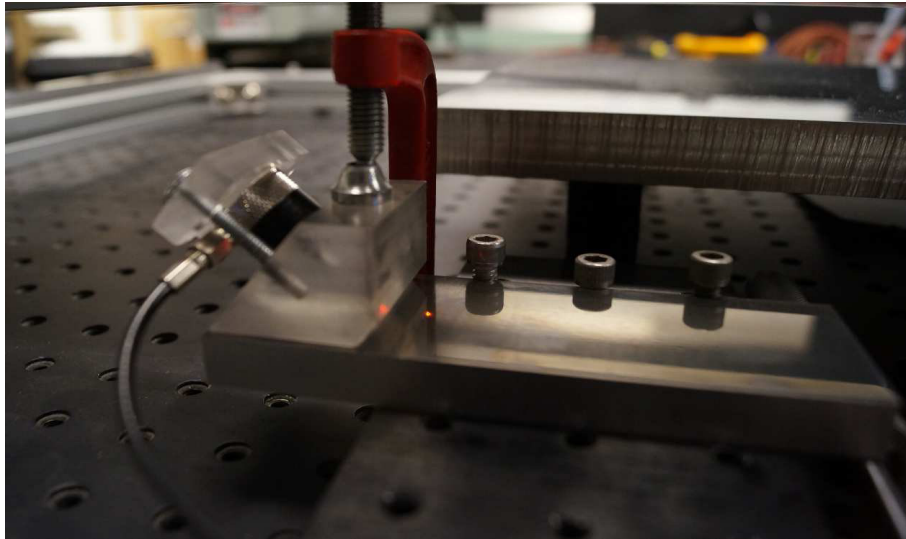


Figure 4.7: Piezoelectric transducer and wedge mounted on the sample

SIGNAL PROCESSING

This chapter introduces the theoretical approach for the demodulation of a frequency modulated signal. Based on Moreau [15], it can be shown that the output of an ideal heterodyne interferometer does not contain any even harmonics of a signal-frequency acoustic signal. Odd harmonics, however, are produced in calculable amounts. To obtain the message signal quadrature modulation and zero-cross detection were applied to measure the fundamental and second harmonic amplitude. Furthermore, these application were optimized for a non ideal heterodyne interferometer. Quadrature modulation provides a theoretical spectrum analysis. Zero-cross detection is a far more straight forward method can be implemented to recover the message signal.

5.1 Demodulation

As derived in Chapter 3, the frequency modulated can be expressed in terms of Bessel functions

$$V_d = \sum_{n=-\infty}^{\infty} J_n(\zeta) \cos(\omega_B t + n\omega_u t), \quad (85)$$

where $f_B = 40MHz$ and $f_u = 2.1MHz$. Equation 85, contains a carrier frequency and an infinite amount of sideband. We can extract the carrier signal from the message signal, by a sinusoidal mixer and apply it on V_d . Thus,

$$V_u = V_d \sin(\omega_B t) = \sum_{n=-\infty}^{\infty} J_n(\zeta) \sin(\omega_B t) \cos(\omega_B t + n\omega_u t). \quad (86)$$

By using the addition theorem $\sin(x) \cos(x) = \frac{1}{2}(\sin(x - y) + \sin(x + y))$, we can expand modulated signal V_u , into

$$V_u = \frac{1}{2} \sum_{n=-\infty}^{\infty} J_n(\zeta) (-\sin(n\omega_u t) + \sin(2\omega_B t + n\omega_u t)). \quad (87)$$

Now we can eliminate the energy of the carrier with a 15 MHz lowpass filter

$$V_u = -\frac{1}{2} \sum_{n=-\infty}^{\infty} J_n(\zeta) \sin(n\omega_u t). \quad (88)$$

Since $f_B/f_u \approx 0.0525$, we can assume that we are dealing with a narrowband signal. By applying the properties of the Bessel functions given in Chapter 3.2.3, we gain the demodulated signal, such that

$$V_u = - \sum_{n=-1, s \text{ odd}}^{\omega_c/\omega_m} J_s(\zeta) \sin(n\omega_u t). \quad (89)$$

Equation 89, shows that only odd harmonics are being created and therefore, it doesn't artificially increase the nonlinearity parameter β .

5.2 Nonideal Interferometer

In reality there are many potential sources which are the cause a spurious increase of second harmonics. Figure 5.1, shows a measured raw signal, captured by the oscilloscope. It can be observed that the signal output is both frequency and amplitude modulated.

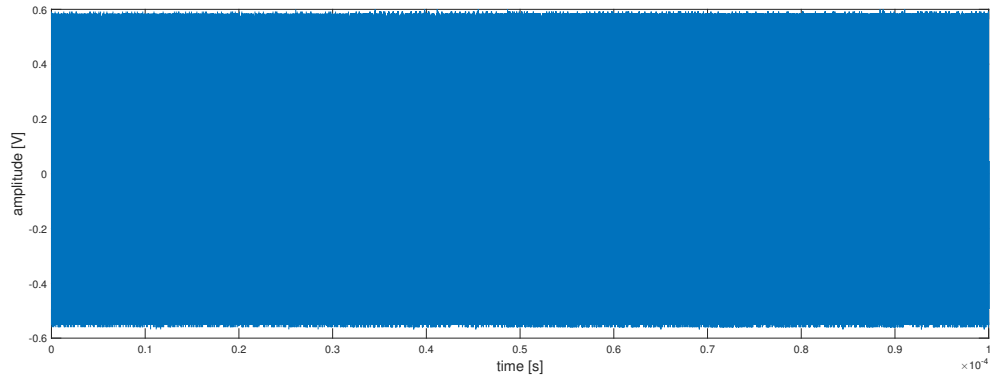


Figure 5.1: Raw signal

5.2.1 Quadrature demodulation

Mixers are highly non-linear elements which effect the fundamental and the second harmonic amplitude significantly because of their DC component. Their influence is crucial, especially in combination with the time varying angle phase-shift with the constant value α . In order to study the nature of this phase-shift, we need to include the it into Equation 85. Thus,

$$V_{d1} = \sum_{n=-\infty}^{\infty} J_n(\zeta) \cos(\omega_B t + n\omega_u t + \alpha). \quad (90)$$

By applying the mixer

$$V_{u1} = V_{d1} \sin(\omega_B t) = \sum_{n=-\infty}^{\infty} J_n(\zeta) \sin(\omega_B t) \cos(\omega_B t + n\omega_u t + \alpha), \quad (91)$$

and noting that $\sin(x) \cos(x) = \frac{1}{2}(\sin(x - y) + \sin(x + y))$, it follows that the demodulated output is

$$V_{u1} = \frac{1}{2} \sum_{n=-\infty}^{\infty} J_n(\zeta) (-\sin(n\omega_u t + \alpha) + \sin(2\omega_B t + n\omega_u t + \alpha)), \quad (92)$$

which can be again simplified into

$$V_{u1} = -\frac{1}{2} \sum_{n=-\infty}^{\infty} J_n(\zeta) \sin(n\omega_u t + \alpha), \quad (93)$$

with a Low pass filter. For a narrowband signal we can express the function as it follows

$$V_{u1} = -\frac{1}{2} J_1(\zeta) \cos(-\omega_u t + \alpha) + \frac{1}{2} J_0(\zeta) \cos(\phi) + \frac{1}{2} J_1(\zeta) \cos(\omega_u t + \alpha) \quad (94)$$

which can be rewritten as

$$V_{u1} = -J_1(\zeta) \sin(\omega_u t) \sin(\zeta) + \frac{1}{2} J_0(\zeta) \cos(\alpha). \quad (95)$$

Equation 100, consists two components: $\frac{1}{2} J_0(\zeta) \cos(\alpha)$ is a DC component generated by the mixer. $-J_1(\zeta) \sin(\omega_u t) \sin(\zeta)$ represents the message signal with a multiplication of $\sin(\zeta)$. Hence, the amplitude of the fundamental is dependent on the phase error. For a value $\alpha = 0$, this phase error eliminates the energy of the message signal completely, see Figure 5.3. However, the phase shift can be eliminated by a demodulation technique, called quadrature demodulation. To derive the function of the quadrature demodulator, the received signal must be also mixed with $\cos(\omega_B t)$, see Figure 5.2.

Similarly to Equation 94, for a $\cos(\omega_B t)$ mixed signal, the frequency modulated output can be expressed as

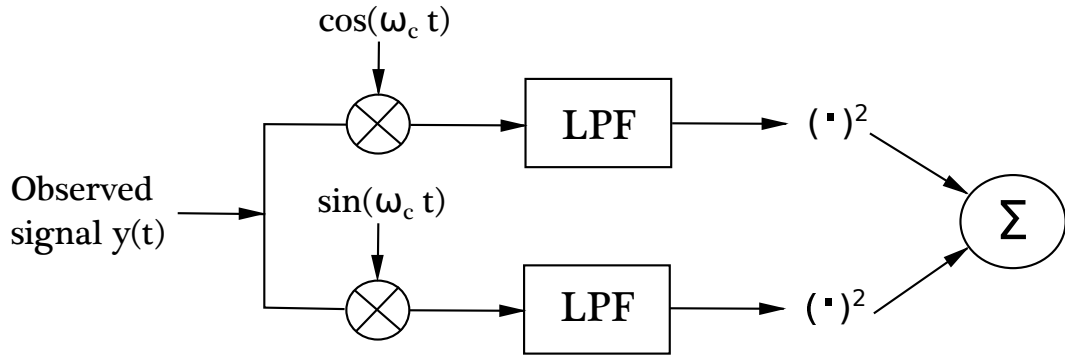


Figure 5.2: Schematics of the quadrature demodulation

$$V_{u2} = V_{d1} \cos(\omega_B t) = \frac{1}{2} J_0(\zeta) \cos(\phi) - J_1(\zeta) \sin(\omega_u t) \sin(\phi) + \frac{1}{2} \sum_{n=-\infty}^{\infty} J_s(\zeta) \cos(2\omega_B t + n\omega_u t + \phi). \quad (96)$$

By using the same filter and same simplifications as for V_{u1} we gain

$$V_d \cos(\omega_B t) = -J_1(\zeta) \sin(\omega_u t) \sin(\alpha). \quad (97)$$

Therefore, the quadrature demodulation approach

$$(V_d \sin(\omega_B t))^2 + (V_d \cos(\omega_B t))^2 = J_1(\zeta)^2 \sin(\omega_u t)^2, \quad (98)$$

can successfully recover the frequency modulated signal and eliminate the phase error. However, taking the root of $(V_d \sin(\omega_B t))^2 + (V_d \cos(\omega_B t))^2$ creates an absolute representation of the message signal. Therefore, it is only possible to observe the quadrature of the spectrum and measure the square of the fundamental and second harmonic.

5.2.2 Zero-cross detection

Another possible way to demodulate a frequency modulated signal is to estimate the instantaneous frequency by using zero-cross detection. It is one of the most common measuring the frequency of the period of a periodic signal. Since the detected signal has a limited time resolution the zero-crossing point needs to be calculated by using the interpolation

$$\Delta t = \frac{x[n]}{x[n] - x[n-1]}, \quad (99)$$

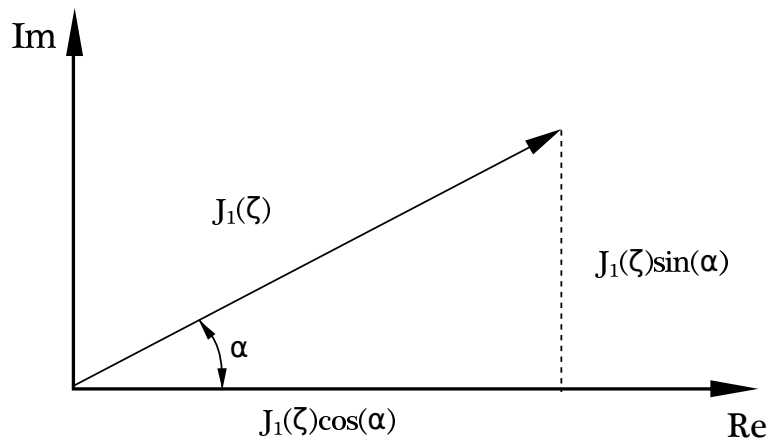


Figure 5.3: Complex projection of the fundamental amplitude

between two points close to zero, see Figure 5.4. We can receive the two closet points to zero by monitoring the sign of the discrete voltage signal. By using a lowpass filte, the high frequency portion can be eliminated. Unlike quadrature demodulation, where we analyze only the spectrum, the zero-cross detection demodulation scheme can reproduce the message signal. Furthermore, amplitude modulation doesn't impact the signal since we ignore the peaks and focus on zero axis.

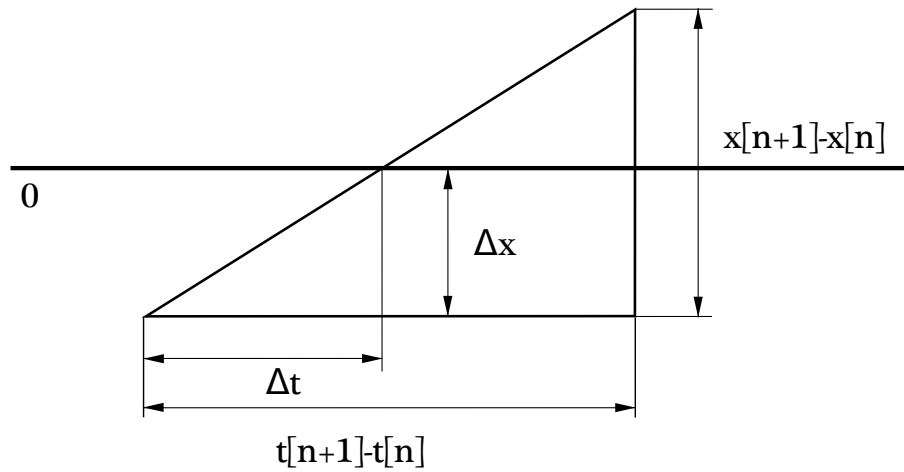


Figure 5.4: Interpolation between two sample points

DATA ACQUISITION AND EXPERIMENTAL RESULTS AND INTERPRETATION

Two completely distinct demodulation techniques, obtained from the same experimental setup are shown and explained in Section 5.2 and 5.3. This chapter summarizes the results obtained from each demodulation technique, followed by an interpretation to establish a relationship between the two demodulation techniques.

6.1 *Output Signal*

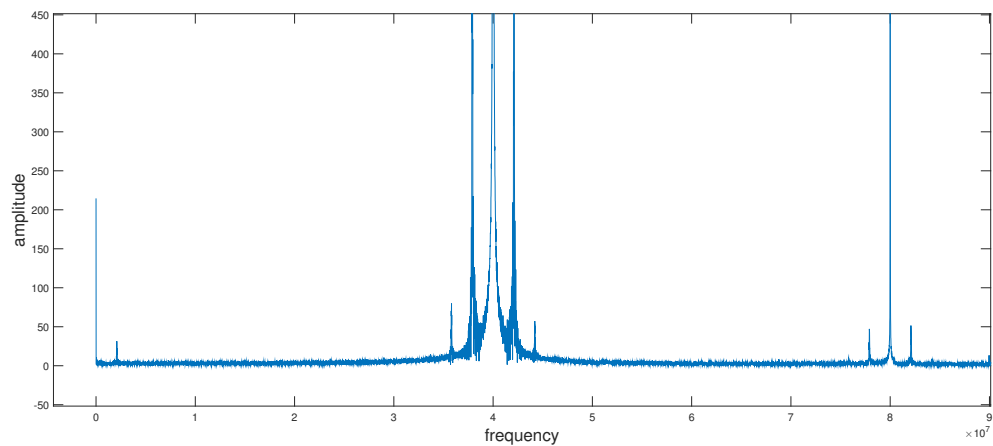


Figure 6.1: Spectrum of the raw signal

Figure 6.1, shows the spectrum of a measured signal modulated a 40MHz Bragg cell and detected by an oscilloscope. It can be observed, that the greatest energy lies at the frequency of 40MHz . Due to an offset in the oscilloscope the spectrum also contains a DC component which can be removed by subtracting the mean value of the detected signal. Figure 6.5, shows an example of a demodulated signal and it can be seen that only a small window contains the sinusoidal toneburst signal. It is important to neglect the spurious signals created by the wave reflection inside of the wedge, since they increase the nonlinearity artificially. The signal also contains an amplitude modulation [15] which can be removed

by expressing Equation 89 as a Fourier expansion of a square wave

$$V_{sq} = \frac{4}{\pi} \sum_{n=-1, n \text{ odd}}^{\omega_c/\omega_m} \sum_{n=-\infty}^{\infty} \frac{J_s(n\zeta)}{n} \sin(n\omega_B + s\omega_u)t. \quad (100)$$

6.2 Quadrature demodulation scheme

The mixer is a fundamental component of the quadrature demodulation technique. Unfortunately, mixers are also highly nonlinear devices that also produce harmonic distortion [20]. It has a high influence on amplitude modulation and a phase-shift. Figure 6.2, shows a magnified snapshot of the measured raw signal and its phase-shift, which changes at a time varying angle. Note that the signal also carries signals from the reflected waves inside of the wedge and a DC-component from the oscilloscope. Both have to be removed before mixing the raw signal with sinusoidal signal.

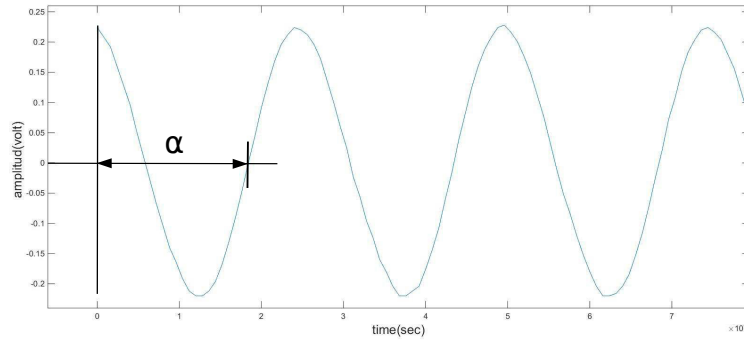


Figure 6.2: Phase error of the measured signal

Figure 6.3, shows the spectrum of a mixed signal. At a frequency of 2.1MHz we can see the fundamental followed by the second harmonic at a frequency of 4.2MHz . As it was mentioned, the fundamental amplitude and therefore also the second harmonic is influenced by the phase-shift. By using the theoretical approach, provided in Chapter 5.2.1, the phase-shift α can be eliminated.

Therefore we can compute the first and second harmonic, as well as A_2/A_1^2 over the propagation distance for a quadrature demodulated signal, see Figure 6.4. However this demodulation process is quite time consuming, since every position needs to be evaluated

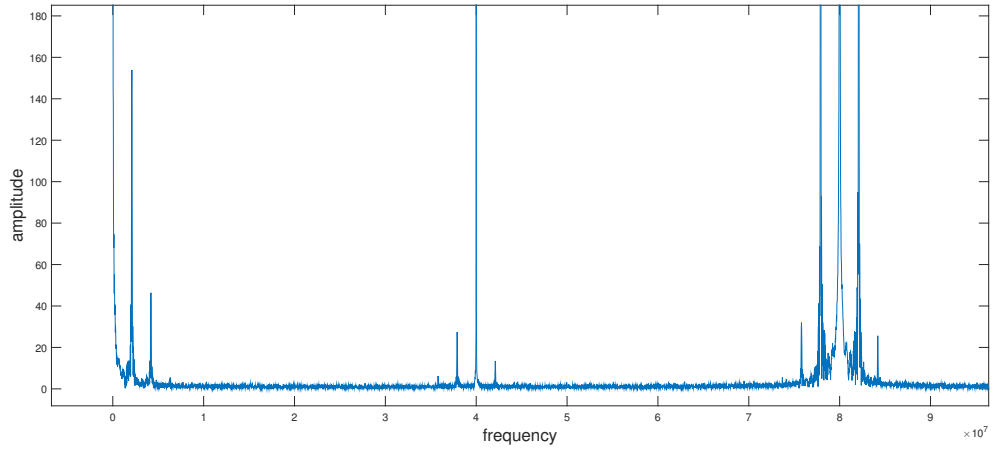


Figure 6.3: Spectrum of a mixed signal

manually for the fundamental and second harmonic. For this research every measured point over the propagation was averaged 32 times for 3 different measurements.

6.3 Zero-crossing detection demodulation scheme

Since we track only the values at zero, the sampling rate will be reduced and it is dependent on the carrier frequency. For a carrier frequency of $f_B = 40MHz$ and a message frequency of $f_u = 2.1MHz$, we reduce the sampling rate to 38 samples per cycle. The influence amplitude modulation is negligible due to the nature of this demodulation process. Also the phaseshift can be neglected since the gained zero-crossing points can be manipulated to $\alpha = 0$, which makes it very simple to recover the message signal

Each measurement taken via the measurement point is being recorded and averaged 128 time in Matlab after the demodulation. A representative time-domain plot is displayed in Figure 6.5, with a steady state portion identified by applying Hann-window to remove the ringing effects in the beginning and in the end.

The windowed signal shown as red function isolates the steady state portion of the signal and is transformed into frequency domain using a fast Fourier Transform. Due to the low resolution of the zero-cross detection demodulation scheme, we need to zero-pad the recovered message signal to obtain an accurate estimate of the amplitude of a sinusoidal signal. The amplitudes of the frequency domain plot represent the A_1 and A_2 , see Figure 6.6. This

procedure has been conducted for 3 different measurements. Therefore, we gain the results, see Figure 6.7

6.4 Comparison of the Results

The nonlinear ultrasound experimental measurements are conducted as explained in detail in Chapter 4. The two different digital demodulation techniques were both applied on the same specimen with similar conditions and the same data set, as explained in Chapter 5. By comparing the results depicted in the Figures 4.4, 6.4 and 6.7, it can be observed that the fundamental amplitude A_1 along the propagation distance has a very similar behavior. Therefore it can be concluded that the demodulation techniques introduced in Chapter 5, are able to successfully demodulate the signal and display the fundamental energy of the message signal over the propagation axis. However, the second harmonic energy A_2 , over propagation distance does not increase nor decrease. As it was stated in Chapter 2, an increase in propagation distance should result in higher amplitudes of the second harmonic [9]. However, A_2 over propagation distance has a stable behavior. It can also be noticed that both demodulation schemes provide an almost identical second harmonic over propagation distance curve, see Figure 6.4 and 6.7. One of the biggest disadvantages of interferometric techniques is the reduction in sensitivity, which can create problems in the detection of any nonlinear behavior. The second harmonic is usually hidden in the wideband noise [15]. The Polytec Helium-Neon laser provides a high resolution and broad bandwidth up to $24MHz$. With a Bragg frequency of $f_B = 40MHz$ and a message frequency of $f_u = 2.1MHz$ and applying it into Equation 84, the needed bandwidth to detect 98% energy is approximately $2.2103MHz$. Therefore, it can be assumed that the bandwidth provided by the laser is sufficient. However, in the experiments conducted in this research the received signal contains a certain noise, which increases overall energy in the signal. Thus, it is necessary to increase the signal to noise ratio as much as possible, so that the energy does not lie in the noise. Due to the surface conditions however, only a part of the laser energy can be obtained back by the receiver. Apart from that, the second harmonic energy is concentrated at a frequency of $4.2MHz$ and it consists less than a tenth of the

energy of the fundamental amplitude. It can be assumed, that the constant second harmonic over propagation distance observed by using the demodulation schemes, is generated by the system nonlinearity and noise. Naturally, the ratio A_2 over $(A_1)^2$ increases due to the stable behavior of A_2 and the decrease of A_1 over the propagation distance. This, increase of the nonlinearity parameter β however, cannot be used as an indicator for the material nonlinearity since it is only generated by the decrease of the fundamental amplitude along the propagation distance.

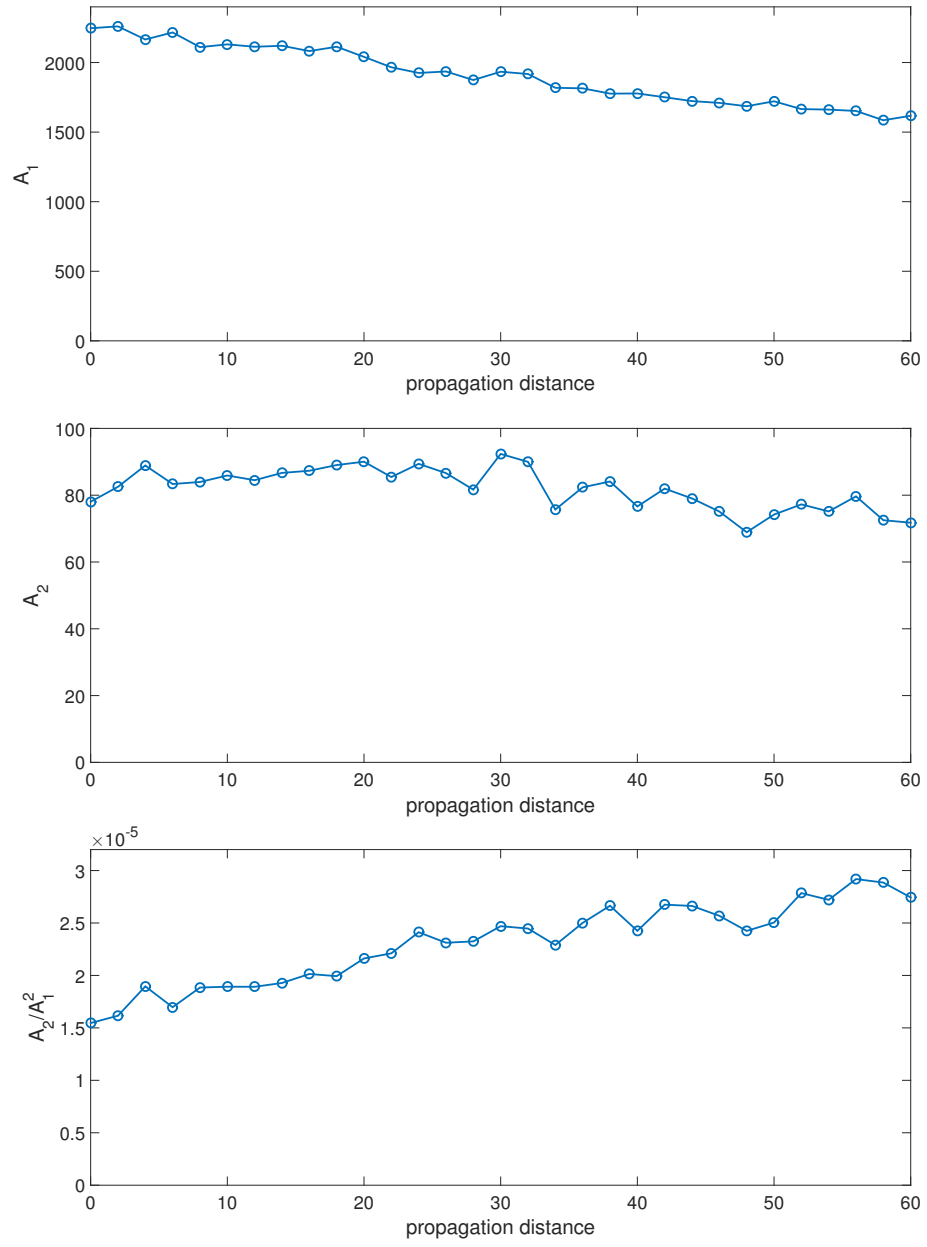


Figure 6.4: Results for a quadrature demodulated signal

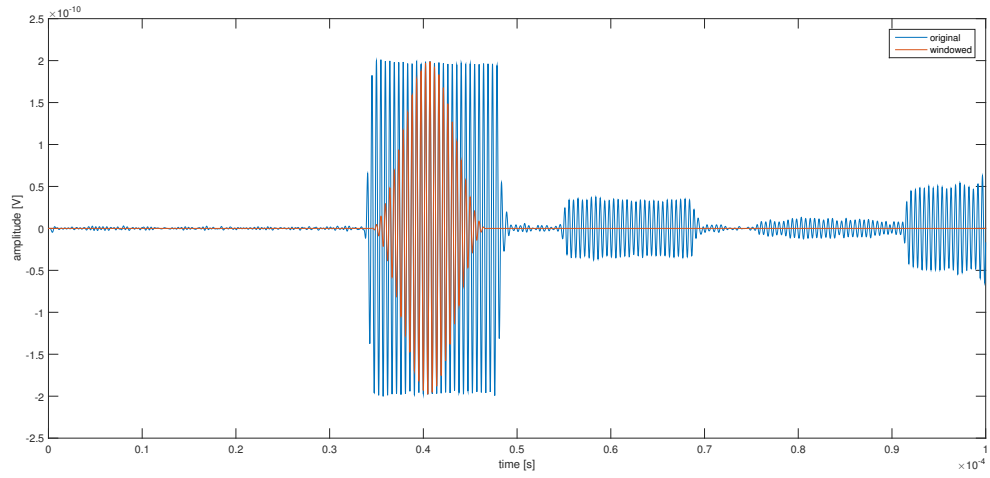


Figure 6.5: Demodulated time-domain signal showing 30 cycles of a received Rayleigh surface wave along with an approximate Hann window

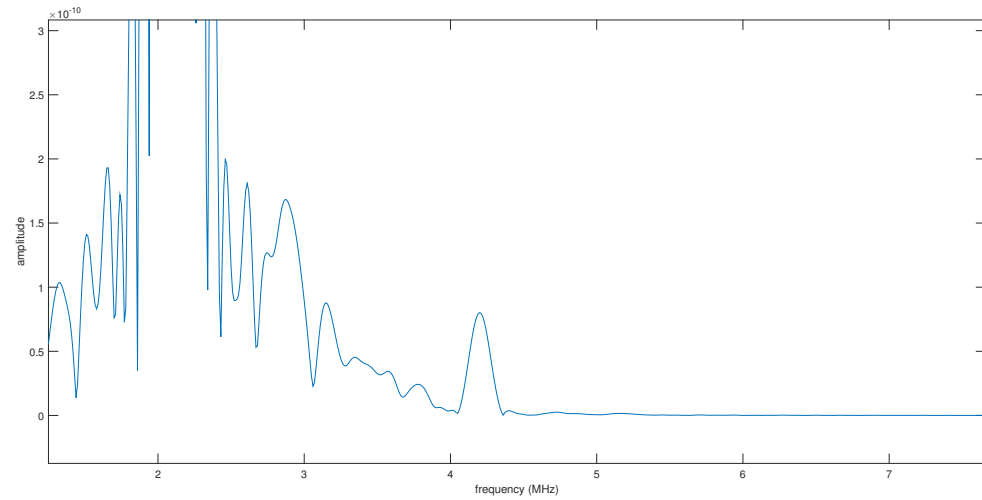


Figure 6.6: Demodulated frequency-domain signal of a received Rayleigh surface wave

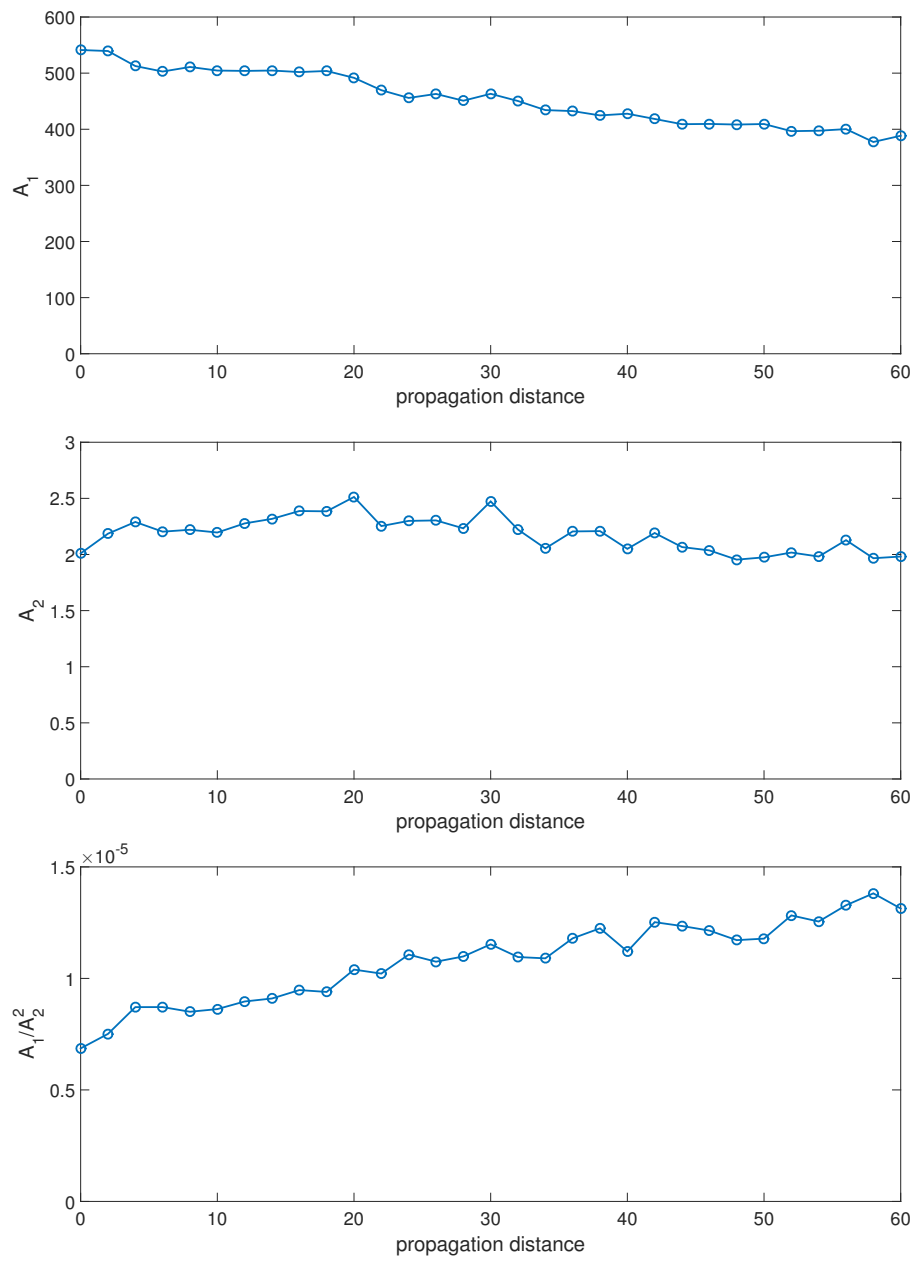


Figure 6.7: Results for a zero-crossing demodulated signal

CONCLUSION AND POSSIBLE IMPROVEMENTS

In this research Rayleigh surface waves are generated with the contact wedge method, to develop a field applicable technique for ultrasonic evaluation of near surface damage. The second harmonic generation method is found to be generally promising, since the fundamental and the second harmonic amplitudes could be detected simultaneously. The second harmonic generation method also demonstrates further advantages like the averaging effect over a finite area for the transmitting signal as well as its detection. This research describes experimental setup and investigates two distinct suitable demodulation schemes. The Fast Fourier Transformation algorithm separates the the second harmonic from the fundamental and the amplitudes are estimated by using zero padding. Quadrature demodulation and zero-cross detection, both provide the necessary properties to eliminate all the influences by a non-ideal interferometer. A comprehensive explanation of the results is given, which considers the theory background and experimental setup. Both demodulation schemes provide precise results for the fundamental amplitude over the propagation distance. Despite the fact that both demodulation techniques provide similar results for the second harmonic, we cannot conclude a relationship between the steady curve of A_2 along the propagation distance and the material nonlinearity. However, it can be assumed that the second harmonic is generated by the system nonlinearity and noise. One of the biggest disadvantages of a LDV is the limited bandwidth. Since the second harmonic is usually hidden in the wideband noise it is very important preserve a high signal to noise ratio. However, due to instrumental limitations the same demodulation techniques could not be applied to a different He-Ne laser with a higher bandwidth. For future work on this method it is recommended to use a laser which provides a broader bandwidth. It is also recommended to enhance the surface conditions and therefore, the signal to noise ratio by using a polishing machine. In order to estimate the lowest absolute displacement level our laser can detect,

a reference measurement with longitudinal waves can be applied, where the fundamental amplitude is measured for increasing driving voltage.

REFERENCES

- [1] *OFV-534 Compact Sensor Head*.
- [2] A. A. GEDROITZ, V. A. K., “Elastic waves of finite amplitude and deviations from hook’s law,” *Sov. Phys. JETP (Engl. Transl.)*, vol. 16, pp. 229–236, 1963.
- [3] A. HIKATA, B. B. C. and ELBAUM, C., “Dislocation contribution to the second harmonic generation of ultrasonic waves,” *Journal of Applied Physics*, vol. 36, p. 229, 1965.
- [4] ACHENBACH, J. D., *Wave Propagation in Elastic Solids*. Elsevier Science Publishers B.V., 1973.
- [5] CANTRELL, J. H., “Substructural organization, dislocation plasticity and harmonic generation in cyclically stressed wavy slip metals,” *Proc. R. Soc. Lond. A.*, pp. 757–780, 2004.
- [6] CANTRELL, J. H. and ZHANG, X.-G., “Nonlinear acoustic response from precipitate-matrix misfit in a dislocation network,” *Journal of Applied Physics*, vol. 68, pp. 5469–5472, 1998.
- [7] GRAFF, K. F., *Wave Motion in Elastic Solids*. Oxford University Press, 1975.
- [8] HAMILTON, M. F. and BLACKSTOCK, D. T., *Nonlinear Acoustics*. Plenum Press New York, 1988.
- [9] HERRMANN, J., “Generation and detection of higher harmonics in rayleigh waves using laser ultrasound,” Master’s thesis, Georgia Institute of Technology, 2006.
- [10] HURLEY, D. C., “Nonlinear ultrasonic assessment of precipitation hardening in astm a710 steel,” *Journal of the Acoustical Society of America*, vol. 106, pp. 1782–1788, 1999.
- [11] KENNEDY, G., *Electronic Communication Systems*. McGraw-Hill, 1985.
- [12] M. A. BREAZEALE, D. O. T., “Finite-amplitude ultrasonic waves in aluminum,” *Appl. Phys. Lett.*, vol. 3, pp. 77–78, 1963.
- [13] M. A. BREAZEALE, J. F., “Ultrasonic studies of the nonlinear behaviour of solids,” *J. Appl. Phys.*, vol. 36, pp. 3486–3490, 1965.
- [14] MARINO, D., “Using nonlinear ultrasound measurements to assess the stage of thermal damage in modified 9thesis, Georgia Institute of Technology, 2014.
- [15] MOREAU, A., “Detection of acoustic second harmonics in solids using a heterodyne laser interferometer,” *National Research Council of Canada*, vol. 75, 1995.
- [16] OPPENHEIM, A. V. and SCHAFER, R. W., *Discrete-Time Signal Processin*. Pearson, 2010.

- [17] THIELE, S., KIM, J.-Y., QU, J., and JACOBS, L. J., “Air-coupled detection of non-linear rayleigh surface waves to assess material nonlinearity,” *Ultrasonics*, vol. 54, pp. 1470–1475, 2014.
- [18] VIKTOROV, I. A., *Rayleigh and Lamb Waves, Physical Theory and Applications*. Plenum Press New York, 1967.
- [19] YOUNG, P. H., *Electronic Communication Techniques*. Prentice Hall, 1985.
- [20] ZIEMER, R. E. and TRANTER, W. H., *Principles of Communications*. Houghton Mifflin Company, 1990.